

Computational Fluid Dynamics
Dipartimento di Scienze e Tecnologie Aeroespaziali
Politecnico di Milano

POLAR OF A 2D GLIDER AIRFOIL: OPTIMIZATION AND EFFECT OF ROUGHNESS

Mohamed Mady (Optimitzation)
Francesco Libretti (Optimitzation)
Alessandro Strambaci (Optimitzation)
Juan Monmeneu (Roughness)
Nil Couto (Roughness)



Contents

| | | |
|----------|--|-----------|
| 1 | Summary | 1 |
| 2 | Problem definition and background | 2 |
| 2.1 | Overview of the topics | 2 |
| 2.1.1 | Optimization | 2 |
| 2.1.2 | Roughness | 2 |
| 2.2 | Theoretical background | 3 |
| 2.2.1 | Governing equations | 3 |
| 2.2.2 | Law of the wall | 4 |
| 2.2.3 | Optimization | 5 |
| 2.2.4 | Roughness extensions for turbulence models | 6 |
| 3 | Design of Experiment | 7 |
| 3.1 | Grid convergence | 7 |
| 3.2 | Optimization | 7 |
| 3.3 | Roughness | 8 |
| 4 | Computational model | 9 |
| 4.1 | Problem geometry and setup | 9 |
| 4.1.1 | Optimization | 10 |
| 4.1.2 | Roughness | 10 |
| 4.2 | Mesh generation and description | 11 |
| 4.2.1 | Grid convergence index | 11 |
| 4.2.2 | Farfield independence | 11 |
| 4.2.3 | Domain discretization | 12 |
| 4.3 | Numerical schemes | 13 |
| 5 | Results | 15 |
| 5.1 | Mesh convergence | 15 |
| 5.2 | Polar | 17 |
| 5.2.1 | $Re = 61400$ | 17 |
| 5.2.2 | $Re = 203100$ | 18 |
| 5.2.3 | Flow structure at $\alpha = 2^\circ$ | 19 |

| | | |
|----------|--|-----------|
| 5.3 | Law of the wall | 21 |
| 5.3.1 | SA model | 21 |
| 5.3.2 | SST model | 22 |
| 5.4 | Optimization | 23 |
| 5.5 | Roughness | 26 |
| 5.5.1 | Fully rough airfoil | 26 |
| 5.5.2 | Effects of localized roughness | 29 |
| 6 | Conclusions | 32 |
| 6.1 | Optimization | 32 |
| 6.2 | Roughness | 32 |
| 7 | Appendix A: Resources | 36 |

1. Summary

This report presents a comprehensive study of the application of the discrete adjoint method for the optimization of the drag coefficient in order to maximize the efficiency of a NACA 6409 airfoil section, and a study of the effect of applying surface roughness, both on the entire airfoil and localised. First, we perform a mesh convergence test to arrive to a sufficiently grid-independent solution for two Reynolds numbers. Our case of study is governed by incompressible Reynolds-averaged Navier-Stokes equations, and we perform the mesh convergence test for the Spalart-Allmaras and Menter's Shear Stress Transport turbulence models. We then plot the Law of the Wall and simulate the aerodynamic characteristics of the airfoil, comparing them with available experimental data at our test conditions.

Regarding optimization, the lift-to-drag ratio of the NACA 6409 airfoil at two different angles of attack is bench-marked for improvement, constraining the airfoil area and the lift coefficient as constants. Two optimized profiles are developed accordingly, resulting in an increase in lift-to-drag ratio of 0.025% for the lowest angle of attack, and 5.64% for the highest angle of attack.

Regarding roughness, the equivalent sand-grain approach was adopted to simulate the Law of the Wall for the entire rough airfoil with Spallart-Allmaras turbulence model and Bas-Cackmacioglu transition model. Various values of equivalent sand grain roughness height were implemented for a fixed angle of attack and the Law of the Wall was evaluated accordingly at different chord-wise positions along the upper and lower surfaces. Localised roughness was then applied on three chord-wise positions along the upper and lower surfaces and the efficiency was studied for each case. For each combination of angle of attack and roughness position, different values of equivalent sand-grain roughness height were studied.

2. Problem definition and background

2.1 Overview of the topics

The present report is focused on two topics that have been treated independently. On the first stage of the project we collaborated to perform the mesh convergence study that led to the generation of the polar for the NACA 6409 section and Law of the Wall for the baseline case. Afterwards, the topic concerning optimization was carried out by Mohamed Mady, Alessandro Strambaci and Francesco Libretti, while the topic concerning roughness was carried out by Nil Couto and Juan Monmeneu. A brief introduction to each of these topics is presented below.

2.1.1 Optimization

Optimization has long been considered as a means to solve the design problem in a formal and general manner. In the aerodynamic field, one of the main design problems is related a combination of the drag reduction and efficiency improvement in order to achieve better performance and cost reduction; in this paper, a typical glider profile optimization is performed.

Optimization techniques for the design of vehicles generally use gradient-based methods in which the body shape is parameterized with a set of design variables. The aim of the optimization algorithm is the minimization of an objective function (e.g. drag), which requires the computation of the sensitivities of the objective function with respect to the design variables; in fluid mechanics, it is usually demanding since the derivatives of the flow variables, which are solutions of Partial Differential Equations, with respect to the design variables are involved. The computational resources and time required to solve an optimization problem have always been an issue for engineers for a long time, since it requires a huge amount of computational power to obtain the sensitivities; this leads the aerodynamic optimization to be a problem of the second half of the past century. During the years, different methods have been studied, one of them is the discrete adjoint method, which allows to compute the sensitivities in a very efficient way; this method will be explained in Section 2.2.3. The only literature used as a guide for the optimization part consists of the SU2 tutorial [1].

2.1.2 Roughness

The effect of roughness in boundary layers has traditionally been studied and approached experimentally in aerospace applications. Concerning glider and sailplane wings, various experimental studies have been conducted on the effect of implementing turbulent trips (often called turbulators) on the aerodynamic characteristics of the airfoil sections, which is one of the main areas of interest of our project. These studies are relevant inasmuch as gliders tend to show flow patterns typical of the low Reynolds number regimes in which they generally operate. One of these important phenomena is the formation of laminar separation bubbles, formed due to the inability of the boundary layer to transition to turbulent flow in the attached boundary layer. These can have a detrimental effect on the lift to drag ratio as the angle of attack increases due to the increase in wake drag. Furthermore, they eventually become the onset of complete flow separation [2]. Turbulators force

transition and avoid the formation of laminar bubbles, thus reducing wake drag (at the expense of increasing skin friction). The conclusions of these studies are very diverse. On one hand, turbulators are found to reduce drag at high angles of attack and low Reynolds numbers [3]. On the other hand, they cause a gradually greater penalty on drag as the angle of attack lowers and Reynolds increases [4]. In sum, it is frequently concluded that the effect of boundary layer trips is extremely sensitive to Reynolds number, angle of attack, airfoil section, and trip characteristics (height, width, shape, etc) [5].

On the other hand, the numerical implementation and simulation of the effect of roughness has been widely studied in aerospace and energy contexts in the last decades. It is particularly thriving in contexts such as ice accretion, leading edge erosion and surface degradation. These different manifestations of roughness have a profound influence on the velocity profile within the boundary layer, which can ultimately affect the aerodynamic performance of airfoil sections. As a result, they may affect the aeroelastic performance of 3D structures like wings, propellers and wind turbine blades. The complexity and cost of performing experimental studies of these phenomena, together with the versatility and increasing accuracy of CFD software is driving the research front towards numerical simulations.

The most relevant literature to which we will refer along this report concerning the numerical simulation of roughness in the open-source CFD solver SU2 is [6, 7, 8, 9].

2.2 Theoretical background

2.2.1 Governing equations

The Navier-Stokes equations for incompressible flow take the form:

$$\frac{\partial u_i}{\partial x_i} = 0 \quad (2.1)$$

$$\frac{\partial u_i}{\partial t} + \frac{\partial u_i u_j}{\partial x_j} = -\frac{1}{\rho} \frac{\partial p}{\partial x_i} + \nu \frac{\partial^2 u_i}{\partial x_j \partial x_j} \quad (2.2)$$

Substituting each variable ϕ by the average $\bar{\phi}$ and fluctuation ϕ' terms.

$$\phi = \bar{\phi} + \phi' \quad (2.3)$$

Being $\phi(x, t)$ a generic flow variable, it can be written as the sum of its mean ($\bar{\phi}(x, t)$) and fluctuating components ($\phi'(x, t)$), $\phi(x, t) = \bar{\phi}(x, t) + \phi'(x, t)$, then substituting it in the Navier-Stokes equations and taking the time average results in the following Reynolds-averaged Navier-Stokes equations (RANS),

$$\frac{\partial \bar{u}_i}{\partial x_i} = 0 \quad (2.4)$$

$$\frac{\partial \bar{u}_i}{\partial t} + \frac{\partial \bar{u}_i \bar{u}_j}{\partial x_j} = -\frac{1}{\rho} \frac{\partial \bar{p}}{\partial x_i} + \nu \frac{\partial^2 \bar{u}_i}{\partial x_j \partial x_j} - \frac{\partial \bar{u}'_i \bar{u}'_j}{\partial x_j} \quad (2.5)$$

where the term $\bar{u}'_i \bar{u}'_j$ is the Reynolds stress tensor denoted by R_{ij} and was approximated using Boussinesq hypothesis.

2.2.2 Law of the wall

The law of the wall is a universal law of the variation of the velocity profile with the wall distance. Expressions for the velocity profile in the different near wall regions can be obtained in terms of non-dimensional quantities y^+ and u^+ , which are defined as:

$$y^+ = \frac{yu_\tau}{\nu} \quad (2.6)$$

$$u^+ = \frac{u}{u_\tau} \quad (2.7)$$

Where u_τ is the friction velocity defined as:

$$u_\tau = \sqrt{\frac{\tau_w}{\rho}} \quad (2.8)$$

In the viscous sublayer, defined for $y^+ < 5$, viscous shear stress overwhelms Reynolds shear stress. In this region turbulent kinetic energy is transported from the buffer layer ($5 < y^+ < 30$) to the wall by viscous stress, and the relation between u^+ and y^+ becomes linear:

$$u^+ = y^+ \quad (2.9)$$

Provided Re is large enough, an intermediate region exists for $y^+ > 50$ and $y/c \ll 1$ where the logarithmic law of the wall holds:

$$u^+ = \frac{1}{k} \ln(y^+) + C \quad (2.10)$$

Where $k \sim 0.41$ is the Von Karman constant and $C \sim 5.1$ is the additive constant for a clean wall.

Introduction of surface roughness leads to modifications in the velocity profile in the near wall region, and as a consequence it affects aerodynamic coefficients. In order to characterize roughness the equivalent-sand grain approach proposed by Nikuradse [10] has been followed, where real roughness height can be related to an equivalent sand-grain roughness height k_s . When considering roughness, the logarithmic law of the wall for the clean case in Equation 2.10 must be modified, as now it's also function of the non-dimensional equivalent sand-grain roughness height k_s^+ . Thus:

$$u^+ = \frac{1}{k} \ln\left(\frac{y^+}{k_s^+}\right) + B(k_s^+) \quad (2.11)$$

$$k_s^+ = \frac{k_s}{\delta_\nu} \quad (2.12)$$

For this case, following Schlichting's treatment of rough pipes [11], the log-law shift is function of k_s^+ , through the dependency of the logarithmic term in Equation 2.11 and the additive constant B on k_s^+ . According to the value of k_s^+ , different roughness regimes can be identified:

- Smooth regime ($k_s^+ < 5$) : The velocity profile is not modified with respect to the clean airfoil one, as the roughness scale is small compared to viscous scales dominating in the inner wall region. Recovering Equation 2.10 we obtain $B \sim 5.1$.
- Transitionally-rough regime ($5 < k_s^+ < 70$): For this regime the additive constant B is not constant and changes with k_s^+ , displacing the logarithmic region downwards with respect to the clean one described in Equation 2.10.
- Fully-rough regime ($k_s^+ > 70$): The additive constant doesn't depend on k_s^+ anymore as dependency on viscosity drops. Schlichting and Gersten proposed a value for the additive constant $B \sim 8.0$ [11].

2.2.3 Optimization

In the following paragraph, a brief overview of the optimization problem is given; the target is to improve the aero-performance of a surface by searching the local minimum of an object function, which is the drag coefficient for our test case. An optimization problem, incorporating a steady state constraint, can be written as

$$\min_{\alpha} J(U(\alpha), X(\alpha)) \quad (2.13)$$

$$\text{subject to } U(\alpha) = G(U(\alpha), X(\alpha)) \quad \text{and} \quad X(\alpha) = M(\alpha) \quad (2.14)$$

where J is the objective function, U contains the flow variables and X is the flow mesh; in Eq. 2.14 the residual of the flow variable is forced to be null and the flow mesh consistent to the surface mesh M . As can be seen, all this functions are connected to the design variables α .

The optimization problem can be subdivided in four main steps:

- geometry parametrization, done with an interpolation method called Free Form Deformation, in which a box, whose vertices are the design variables, is created around the airfoil.
- RANS simulation.
- calculation of surface sensitivity $\frac{dJ}{d\alpha}^T$, which represents the variable that describe how objective function J changes with a change in the value of each design variable α , done with finite differences, continuous adjoint or discrete adjoint.
- mesh deformation.

The optimization problem is guided by an iterative gradient based method, the Sequential Least SQuare Programming (SLSQP), in which the value of the design variable is update at each iteration as

$$\alpha_{n+1} = \alpha_n - \frac{J(n)}{\text{Jacobian}(n)} \quad (2.15)$$

For this test case, a discrete adjoint method is selected to derive the surface sensitivity of the problem; starting from Eq. 2.14, the Lagrangian associated to this optimization problem is defined as

$$L(\alpha, U, X, \Lambda_f, \Lambda_g) = J(U, X) + [G(U, X) - U]^T \Lambda_f + [M(\alpha) - X]^T \Lambda_g \quad (2.16)$$

where Λ_f contains the adjoint flow variables and Λ_g contains the adjoint geometry variables. If L is differentiated with respect to α , Λ_f and Λ_g can be set in order to make the flow variables and the mesh independent from the design variables, which leads to a PDE for Λ_f and an algebraic equation for Λ_g . Finally, the sensitivity is obtained as

$$\frac{dL}{d\alpha}^T = \frac{dJ}{d\alpha}^T = \frac{dM(\alpha)}{d\alpha}^T \Lambda_g \quad (2.17)$$

As implemented in SU2, the optimization algorithm takes twice the computational cost of a direct simulation and five times the memory required. In comparison, the finite differences algorithm needs a number of simulations equal to twice the number of the design variables.

2.2.4 Roughness extensions for turbulence models

There are two procedures which can be used to model wall roughness in Navier-Stokes computations without solving the flow equations around each roughness point. The first procedure is based on adding extra terms to the flow equations to represent the obstacle due to the roughness and the drag acting on it. This renders the problem's difficulty impractical and thus it is seldomly used [8]. The second procedure is the equivalent sand grain approach, in which the real roughness is mapped into an idealized roughness height k_s , as seen in Section 2.2.2.

SU2 allows to model the implementation of roughness when the equivalent sand grain approach is used. There are various extensions for eddy-viscosity based turbulence models (like SA and SST) which change the eddy viscosity at the wall region, thus changing skin friction and heat transfer. As described by Aupoix and Spalart in [8], these extensions can be classified in two categories depending on the boundary conditions set for the eddy viscosity at the wall:

1. Extensions where the eddy viscosity at the rough wall is zero. Roughness is represented by decreasing the turbulent damping at the wall.
2. Extensions where the eddy viscosity at the rough wall is set to a finite value. A way to picture this is by imagining an additional wall with a certain offset to the original wall, located part-way up the height of the roughness introduced [8]

Roughness extensions exist for the SA and the SST turbulence models. However, in this project we only discuss the extension for SA since it is the only turbulence model used in our simulations with roughness.

The **Boeing roughness extension** was introduced by Spalart in 2000 [9]. It has been successfully implemented, amongst others, by A.K. Ravishankara in 2020 to quantify the effect of roughness on wind turbine blades [7], and by F.A. Caccia in 2021 to predict the effect of icing on horizontal axis wind turbine blades [6]. This extension pertains to the second category described above, where the eddy viscosity at the wall is set to a finite value. Where roughness is applied, the boundary condition for eddy viscosity at the wall $\tilde{\nu} = 0$ is replaced by:

$$\frac{d\tilde{\nu}}{dn} = \frac{\tilde{\nu}}{d} \quad (2.18)$$

where n is a normal along the wall and d is the distance to the nearest wall, which is defined as $d = d_{min} + 0.03k_s$. An offset in wall height is imposed by adding a roughness height of $0.03k_s$ to the minimum distance d_{min} . A value of 0.03 was chosen by Spalart in [9] to fit the fully rough regime. $\tilde{\nu}$ is the modified form of the turbulent kinetic energy in the SA turbulence model. This latter variable is used to define the eddy viscosity as $\nu_t = \tilde{\nu}f_{v1}$. Trimming the value of the viscous damping function $f_{v1} = \frac{\chi^3}{\chi^3 + c_{v1}^3}$ is key to represent correctly the transitionally rough regime. Spalart proposed a shift in $\chi = \frac{\tilde{\nu}}{\nu}$ of:

$$\chi = \frac{\tilde{\nu}}{\nu} + 0.5 \frac{k_s}{d} \quad (2.19)$$

where the value of 0.5 is adjusted so that k_s^+ is in the transitionally rough regime.

3. Design of Experiment

3.1 Grid convergence

Before starting with the resolution of the problem, a mesh convergence is necessary in order to obtain a solution sufficiently independent from the discretization and farfield size; this is done applying the Flux Difference Splitting (FDS), an upwind scheme, and the MUSCL_FLOW option to have a second order scheme. As test cases, two different configurations have been chosen:

- $\alpha = 2^\circ$ for a Reynolds number equal to 61400.
- $\alpha = 6.94^\circ$ for a Reynolds number equal to 203100.

The mesh convergence is achieved in two main steps: firstly, an analysis on the farfield dimensions is done, followed by a study on its discretization. The former is carried out with the SA turbulence model, while the latter is carried out with both SA and SST turbulence models.

Once we arrive to a reasonably mesh-independent solution for the Reynolds numbers and configurations above, the chosen mesh and turbulence model will be used to simulate the aerodynamic characteristics of the NACA 6409 airfoil. In the simulations carried out with the SA turbulence model, we will implement the Bas-Cakmakcioglu transition model (BC) to better ascertain transition effects in our solution, as it will be crucial in further stages of the report. We will plot the following relations with SA and SST:

- Lift Coefficient vs angle of attack
- Drag Coefficient vs angle of attack
- Drag polar

These will be plotted against the experimental data in [12] for comparative purposes.

Finally, the Law of the Wall (LOTW) will be evaluated for the chosen mesh. As will be discussed in Section 5.3 this will motivate the study of the LOTW at higher Reynolds numbers using our computational model setup and solver configuration.

3.2 Optimization

The optimization is carried out with the following models:

- Reynolds-averaged Navier–Stokes (RANS) equations with SA scheme as turbulent model and BC scheme as transition model.
- Jameson-Schmidt-Turkel (JST) scheme as numerical method for the direct and the adjoint simulations.

In order to proceed with the simulation, different SU2 tools are required: `SU2_CFD`, `SU2_DEF`, `SU2_CFD_AD`, `SU2_DOT_AD`, `SU2_GEO` and `shape_optimization.py`. Firstly, a box containing the airfoil is created using `SU2_DEF` by setting the kind of deformation as `FFD_SETTING`; as an additional option, the box has been discretized using 10 control points, as can be seen in Figure 3.1. Secondly, the optimization is run with `shape_optimization.py`, which automates the entire shape design process, by setting the kind of deformation as `FFD_CONTROL_POINT`; as said before, two constraints are imposed on the simulation: the airfoil area is set as constant and equal to 0.0617472 m^2 , value obtained with `SU2_GEO`, and the lift coefficient is forced to be greater than the value calculated with the previously direct simulations. Different parameters have to be set in order to obtain an adequate order of magnitude of several results, such as the deformation of the box and the norm of the gradient.

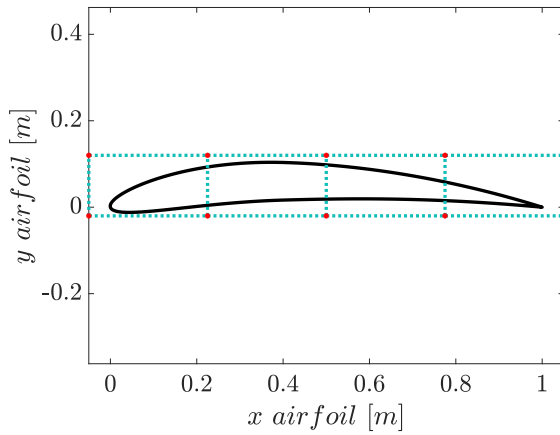


Figure 3.1: FFD box

3.3 Roughness

The objective of this part is to evaluate the effects of roughness in the boundary layer, model and test different turbulent trips in different locations and finally, compare their effects on aerodynamic performance to the clean airfoil's. We will use the RANS equations with SA turbulence model and BC transition model at a Reynolds number of 203100. The steps that we will follow are explained below.

- **Validation:** the first step will be to validate the ability of the mesh obtained in previous steps to correctly model roughness applied to the **whole surface** of the airfoil. To this end, we will plot the Law of the Wall and compare our results to the analytical results introduced in Section 2.2.2 regarding the rough Law of the Wall, described by Equations 2.9 and 2.11. Different values of equivalent sand grain roughness height k_s will be used and the Law of the Wall will be evaluated for these k_s as a function of span-wise position for both upper and lower surfaces. We will compare our results to the data obtained in [6, 7].
- **Testing:** we will then model the implementation of turbulent trips (or turbulators) with different values of k_s and in different positions on the upper and lower surfaces. Finally, we will study C_f plots of the airfoil with the strip and compare them to the clean airfoil's so as to examine any possible changes in the flow structure. By comparing the overall lift-to-drag ratio of the airfoil with the turbulent trip to the clean airfoil's, we will establish if there is any beneficial effect and hypothesize the reasons why (or why not). For more details on the computational model devised for roughness implementation and the methodology of the tests, refer to Section 4.1.2.

4. Computational model

4.1 Problem geometry and setup

The geometry of the NACA 6409 used for the different studies can be seen in Figure 4.1. The airfoil has a chord of $1m$ and its leading edge is placed at the origin of the coordinate system. The computational domain consists on a circle of radius $120m$ centered in the origin of the coordinate system (see Figure 4.2). A further description of the mesh characteristics is presented in Section 4.2

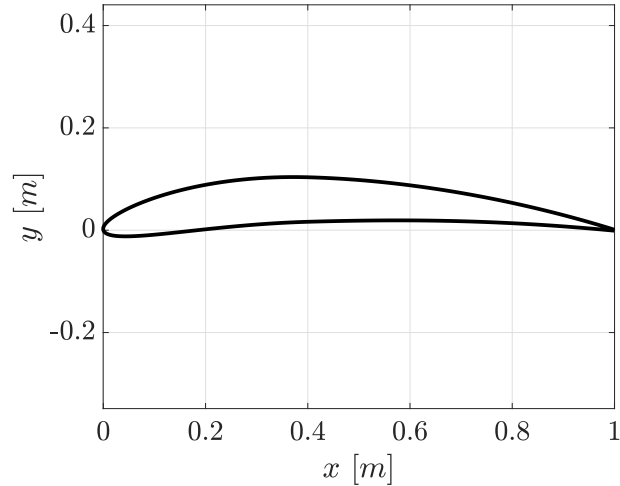


Figure 4.1: NACA 6409

The wall is set to be adiabatic in order to enforce the non-slip condition. Freestream conditions are presented in Table 4.1. The freestream velocity has been selected in order to match the experimental data available for the NACA 6409 airfoil, corresponding to $Re=203100$, available in [12].

| | |
|-------------|---|
| Velocity | 3.0722 m/s |
| Density | 1.225 kg/m^3 |
| Temperature | 288.15 K |
| Viscosity | $1.853 \cdot 10^{-5} \text{ kg/m} \cdot \text{s}$ |

Table 4.1: *Free-stream properties*

4.1.1 Optimization

The objective of the optimization process is to optimize the performance, in terms of drag reduction, of the NACA6409 at two different angles of attack: $\alpha = 2^\circ$ and $\alpha = 7^\circ$, for which the relative aerodynamic coefficients are reported in Table 4.2. The optimization is performed with two constraints imposed on the simulation:

- the airfoil area is set as constant and equal to 0.0617472 m^2
- the lift coefficient is bound to be greater than the values calculated with the direct flow simulations

| $\alpha[\circ]$ | C_L | C_D |
|-----------------|----------|-----------|
| 2 | 0.836871 | 0.0115171 |
| 7 | 1.333423 | 0.0165509 |

Table 4.2: *Aerodynamic coefficients*

4.1.2 Roughness

As was described in Section 3.3, the implementation of roughness in the code is divided in two parts: validation and testing. The simulations for the validation part are performed with the mesh shown in Figures 4.2 and 4.3 with characteristics presented in Section 4.2. The numerical schemes used are described in Section 4.3. For this part, roughness is coded into the *.cfg* file of SU2 with the command `WALL_ROUGHNESS = (MARKER, k_s)`. In this case, the marker to which apply the roughness is `AIRFOIL`, as we want to apply surface roughness to the entire surface. The values of k_s chosen for this purpose are 0.012, 0.006 and 0.001, and the Law of the Wall will be plotted for $x/c = 0.15$, x/c for maximum y -coordinate, and $x/c = 0.7$, for the upper and lower surfaces. We chose these values of k_s to explore the effect on the boundary layer of a wide range of roughness heights. Furthermore, the values of x/c above were chosen to comprise a wide spectrum of C_f values, thus obtaining a representative range of k_s^+ at which to validate the results of the Law of the Wall.

For the testing part however, things change slightly. The mesh, the numerical schemes and the geometry of the airfoil do not change, but additional physical surfaces must be declared in the discretization of the geometry of the airfoil. Additional splines are created from the existing geometry points (which will be associated to the new marker: `STRIP`) where roughness is enforced by setting different values of k_s with the SU2 command `WALL_ROUGHNESS = (AIRFOIL, 0.0, STRIP, k_s)`. The angles of attack tested are 2° , 4° , 6° , 8° , 10° and 12° and the strip width is fixed to 0.1. For the upper surface, the values of k_s chosen for the `STRIP` marker are 0.005 and 0.01, while for the lower surface, the values of k_s chosen for the `STRIP` marker are 0.001, 0.005 and 0.01. We have chosen these values of k_s from trial and error, since we observed that for the full rough airfoil they delivered values of k_s^+ that were in the transitionally rough or fully rough regime. The angle of attack of 4° was chosen since it was observed that it was the angle of attack for maximum efficiency of the baseline case at $Re = 203100$. 2° and 6° were chosen for being the immediately closest angles. 8° , 10° and 12° were chosen since we deemed it relevant to determine the effect that applying the trip at such high angles would cause on the flow pattern, mainly on the laminar separation bubble, which in normal conditions causes a large portion of the flow on the upper surface to separate. We will position the strip on both upper and lower surfaces at different chord-wise positions ranging from $0.25 < x/c < 0.35$, $0.45 < x/c < 0.55$, and $0.70 < x/c < 0.80$. The values above were chosen to evaluate the effect of the turbulence trip on the flow pattern (and thus on the lift-to-drag ratio) at different positions. The width of 0.1 for the `STRIP` marker was chosen since we noticed that thinner trips would sometimes have a negligible effect in some combinations of chord-wise position and

angle of attack.

4.2 Mesh generation and description

4.2.1 Grid convergence index

The grid convergence index (GCI) is an equivalent error due to discretization, expressed as a percentage, which is associated to the upper and lower bound on the deviation of a numerical results with respect to the exact solution, as a consequence of the problem discretization. The computation of the GCI was performed following the procedure laid out by F.A.Caccia described in [6]. A minimum of three grids, with an increasing number of elements, is recommended. The grid refinement factor is defined as:

$$r_{ji} = \frac{h_j}{h_i} \approx \sqrt{\frac{N_i}{N_j}} \quad (4.1)$$

where h_i indicates the average cell size of the mesh i , and h_j refers to mesh j . The grid refinement factor can be approximated as the square root of the number of the elements in the grid. This ratio has to be greater or equal to 1.3. Let us consider three grids h_1, h_2, h_3 , with $h_1 < h_2 < h_3$, and $\epsilon_{32} = \phi_3 - \phi_2$ and $\epsilon_{21} = \phi_2 - \phi_1$, where ϕ_i is a generic variable associated to mesh i . Now it is possible to estimate the apparent order of convergence p by solving a set of non-linear equations, as indicated in [6]. The final steps involve the Richardson extrapolation, in order to determine the value of ϕ as $h \rightarrow 0$, and compute the GCI as

$$GCI_{21} = FS \frac{e_a^{21}}{r_{21}^p - 1} \quad (4.2)$$

with FS being a safety factor of 1.25 and the relative error between grids e_a^{21} being

$$e_a^{21} = \left| \frac{\phi_1 - \phi_2}{\phi_1} \right| \quad (4.3)$$

4.2.2 Farfield independence

As mentioned in Section 3.1 the grid convergence procedure consists of two steps: the assessment of the farfield dimension and the study of the discretization effect. The analysis concerning the farfield is divided in two blocks:

- Fixing the value of the characteristic dimension of the elements near the airfoil and setting the size of the edge of the cells on the farfield equal to 1 chord, while the radius of the farfield is increased; the analysis is performed considering an angle of attack equal to $\alpha = 2^\circ$ and a Reynolds number equal to $Re = 61400$. The objective of this study points out the farfield dimension at which 1 chord size element should be adopted. Table 4.3 shows the different meshes' setup.

| Farfield size [m] | Number of Elements |
|-------------------|--------------------|
| 15 | 51239 |
| 30 | 93439 |
| 45 | 150485 |
| 60 | 226341 |

Table 4.3: *Farfield radius and relative number of elements for different meshes*

- As the previous analysis is completed, the cell size of the element on the farfield and the radius of the latter are doubled and halved and the relative error between the results is compared in order to spot the correct combination of that parameters that ensure the simulation to be independent from the farfield

4.2.3 Domain discretization

Once the farfield is set, the generation of three different grids, with an increasing refinement level, is carried out according to the grid convergence index procedure. The mesh consists of a structured boundary layer surrounded by an unstructured grid made up by triangles. The main criteria consists in keeping the ratio between the average cell size related to two consecutive grids almost constant (greater than 1.3) and doubling the number of the elements in the domain. This aim is fulfilled by keeping constant the number of layers in the structured grid, as well as the size of the first cell on the airfoil surface (as shown in table 4.4), and decreasing both the cell size of the elements near the airfoil and the ones of the farfield, in order to maintain basically the same ratio. The meshes' setup are shown in Table 4.5, where h represents the average cell size and H , the size of the element near the farfield.

| | |
|------------------------|-----------|
| Thickness | 0.07 m |
| First cell size | 0.00001 m |
| Ratio | 1.1 |
| Fan number of elements | 30 |

Table 4.4: *Boundary layer mesh properties*

| h [m] | r_{ji} | H [m] | Number of Elements |
|---------|----------|---------|--------------------|
| 1.0809 | / | 5.33 | 38247 |
| 0.8189 | 1.32 | 4 | 66876 |
| 0.6160 | 1.32 | 2 | 120537 |

Table 4.5: *Domain discretization setup*

The final mesh can be seen in Fig. 4.2, with a detail view of the airfoil reported in Fig. 4.3; this mesh presents an expected y^+ value equal to 0.1.

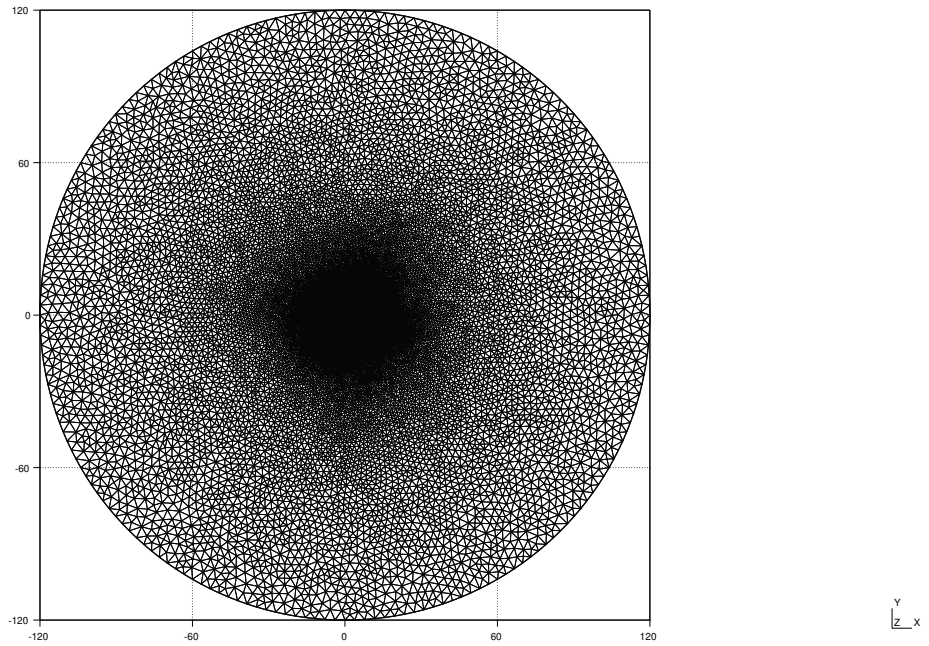


Figure 4.2: Mesh overview

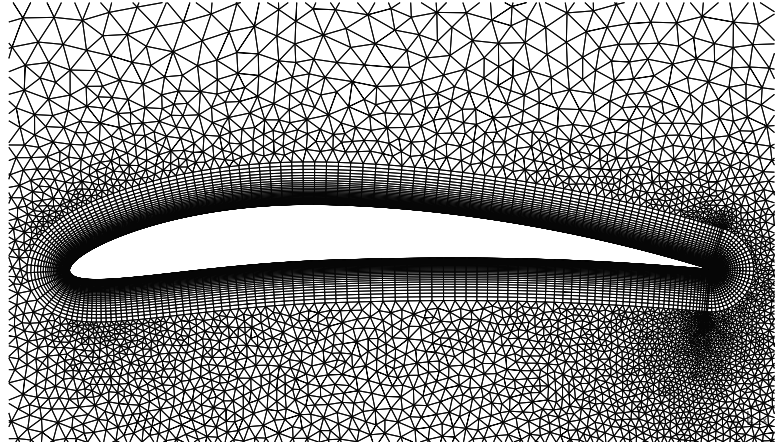


Figure 4.3: Mesh close up view

4.3 Numerical schemes

The case of study is governed by incompressible RANS equations as anticipated in Section 2.2.1, and as a result a turbulent model must be introduced. SA with BC transition model has been selected as the one used with a freestream turbulence intensity value of 0.002. The baseline case was also simulated using SST in order to perform a comparison between both turbulence models. Flow specifications have been computed using conditions in Table 4.1 (note that no model has been used to compute viscosity since it's been set to

constant viscosity). In order to avoid rotating the whole domain, different angles of attack where specified by means of the freestream velocity components. As air is the working fluid, the fluid model corresponds to an ideal gas with ratio of specific heats $\gamma = 1.4$ and specific gas constant $R = 287.7 \text{ J/kgK}$.

The Green-Gauss method has been selected in order to compute spatial gradients, as well as the Euler Implicit method for time discretization. Adaptive Courant–Friedrichs–Lowy number (CFL) has also been implemented, with CFL numbers that range from 25 up to 10^3 . Monotonic Upwind Scheme for Conservation Laws (**MUSC_FLOW** in the *.cfg* file) has been enabled. Therefore, we have used a second order upwind scheme with Venkatakrishnan slope limiter coefficient when using the Flux Difference Spitting (FDS) scheme. The value for the Venkatakrishnan slope limiter ϵ coefficient was obtained following:

$$\epsilon^2 = K_{SU2}^3 \quad (4.4)$$

where K_{SU2} is the threshold parameter. $K_{SU2,2}$ was computed starting from a guess value of $K_{SU2,1} = 0.1$ corresponding to the finest grid and then corrected according to the average cell size of the different grids studied following:

$$\frac{K_{SU2,1}}{K_{SU2,2}} = \frac{\bar{\Delta}_1}{\bar{\Delta}_2} \quad (4.5)$$

The final value obtained for K_{SU2} is 0.1314. The usage of Multi-Grid of level 2 has been implemented in order to speed up the simulations. Regarding convergence, lift coefficient has been selected as the variable for convergence of the solution in all simulations for the mesh convergence analysis and the roughness problem. As a result, a Cauchy series approach has been applied. The solution has been averaged over 100 elements (set with **CONV_CAUCHY_ELEMENTS**) and the solver has been set to stop after the value of said average is smaller than 10^{-5} (set with **CONV_CAUCHY_EPS**). On the other hand, the Root Mean Square error (RMS) of the density is set as the variable for convergence criteria for the optimization problem; a value of 10^{-10} is selected.

5. Results

5.1 Mesh convergence

The results of the two step analysis developed in section 3.1 are shown in Figure 5.1 and Figure 5.2.

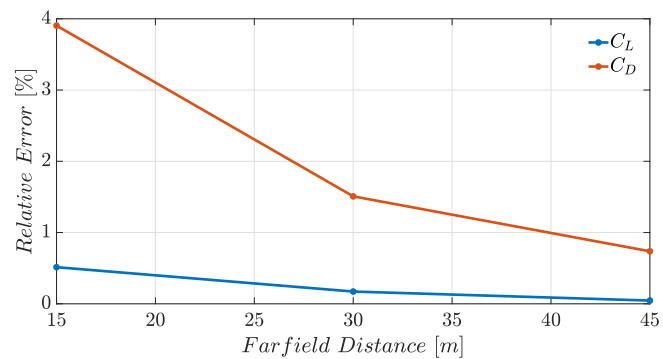


Figure 5.1: Relative error with fixed element size

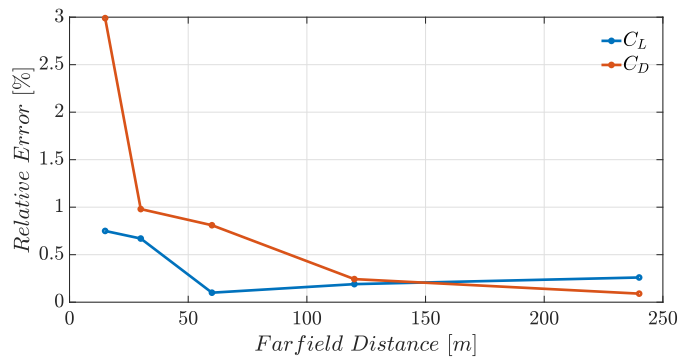
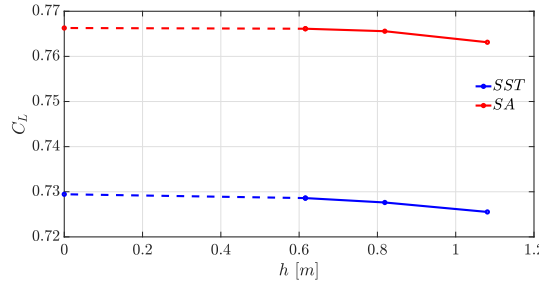
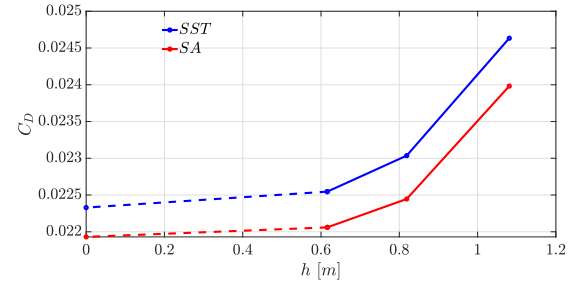


Figure 5.2: Farfield distance analysis

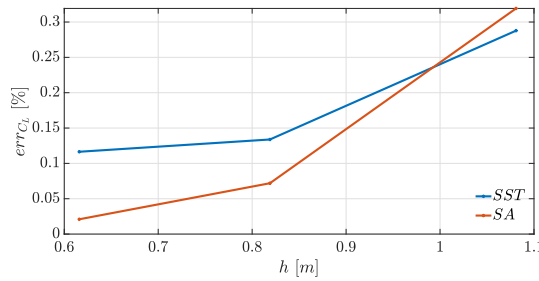
From Figure 5.1 a farfield distance of 30 m is chosen for the one chord size element. Then in Figure 5.2 the relative error is below 0.5% for radius greater than 120 m. Finally a farfield dimension of 120 m with boundary element size equal to 4 m is set. The convergence study in terms of aerodynamic coefficients and their relative errors as a function of average cell size is shown in Figure 5.3 regarding an angle of attack equal to 2° and in Figure 5.4 regarding an angle of attack equal to 6.94°.



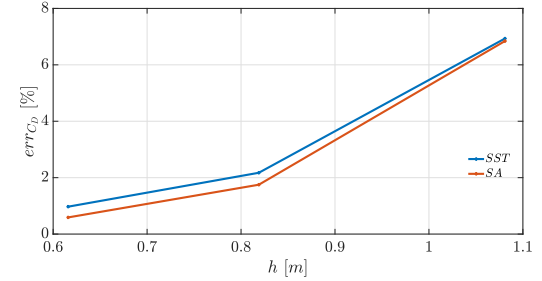
(a) Lift coefficient convergence



(b) Drag coefficient convergence

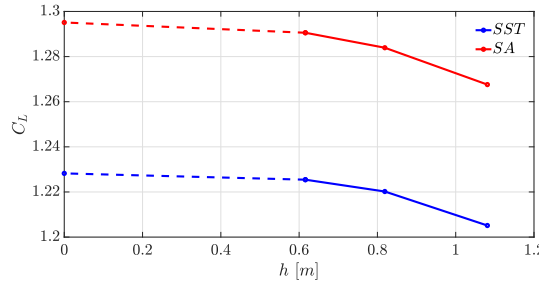


(c) Relative error on lift coefficient

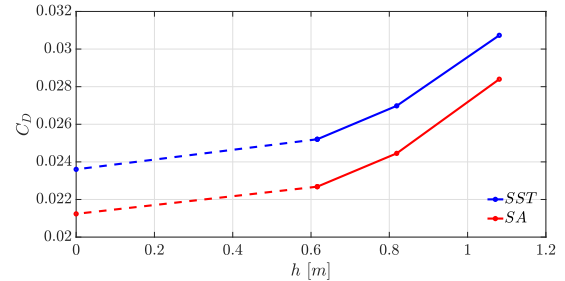


(d) Relative error on drag coefficient

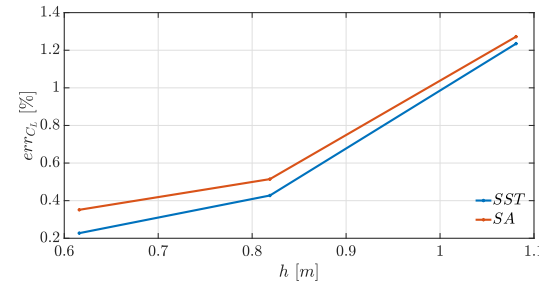
Figure 5.3: $\alpha = 2^\circ$, $Re = 61400$



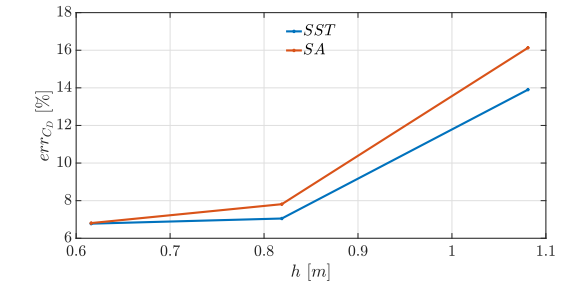
(a) Lift coefficient convergence



(b) Drag coefficient convergence



(c) Relative error on lift coefficient



(d) Relative error on drag coefficient

Figure 5.4: $\alpha = 6.94^\circ$, $Re = 203100$

In Table 5.1 the results in terms of GCI are shown. In order to spare computational resources the medium grid has been used for the rest of the project. The GCI on the medium grid is computed using the relation:

$$GCI_{32} = r_{32}^p GCI_{21} \quad (5.1)$$

| Grid | GCI_{C_L} [%] SA | GCI_{C_D} [%] SA | GCI_{C_L} [%] SST | GCI_{C_D} [%] SST |
|--------|--------------------|--------------------|---------------------|---------------------|
| Fine | 0.0262 | 0.734 | 0.15 | 1.2 |
| Medium | 0.11 | 2.72 | 0.3 | 3.69 |

Table 5.1: *GCI analysis, $\alpha = 2^\circ$, $Re = 61400$*

The error is below the 4% even for the medium grid.

| Grid | GCI_{C_L} [%] SA | GCI_{C_D} [%] SA | GCI_{C_L} [%] SST | GCI_{C_D} [%] SST |
|--------|--------------------|--------------------|---------------------|---------------------|
| Fine | 0.44 | 7.97 | 0.28 | 7.93 |
| Medium | 1.03 | 17.02 | 0.78 | 16.12 |

Table 5.2: *GCI analysis, $\alpha = 6.94^\circ$, $Re = 203100$*

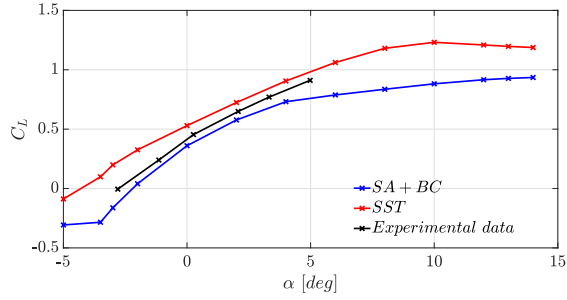
It should be noted that in this case the relative error is larger especially for the medium grid. However, these results derive from a simulation at high angle of attack, where a large portion of the flow over the upper surface is already separated (it starts separating at 40% of the chord). Since the separation region is not negligible, grid convergence can not be achieved by considering a tight bound for the error. For the finest grid the prediction of C_D is in a range of 8%, while for the medium 17%. In order to make comparisons between the baseline solution and the later modifications, by means of roughness and optimization, the medium grid has been finally chosen, since CFD simulations require a huge consumption of memory and CPU time.

5.2 Polar

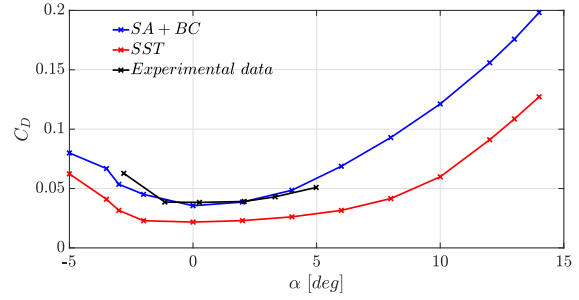
For the aerodynamic data obtained with SU2 and presented in this section, we have benchmarked our simulations to the experimental data for the NACA 6409 airfoil for $Re = 61400$ and $Re = 203100$, obtained from [12].

5.2.1 $Re = 61400$

In Figure 5.5, the aerodynamic coefficients with respect to the angle of attack for the lower Re case are reported, while in Figure 5.6 the relative polar is shown.



(a) Lift coefficient



(b) Drag coefficient

Figure 5.5: Aerodynamic coefficients at $Re = 61400$

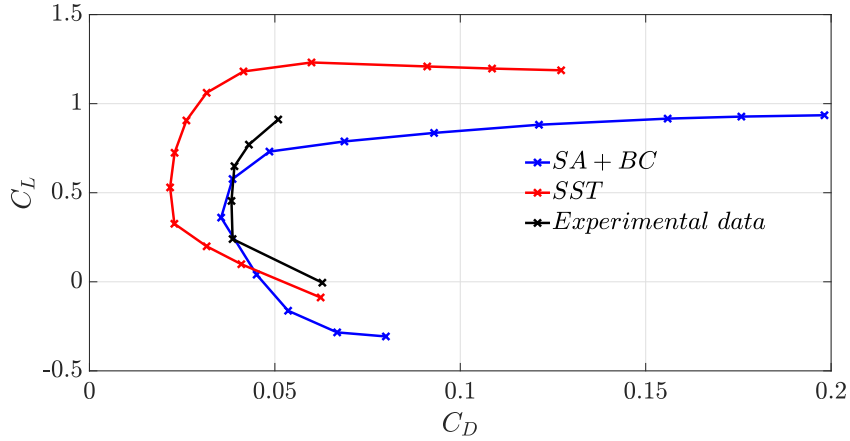
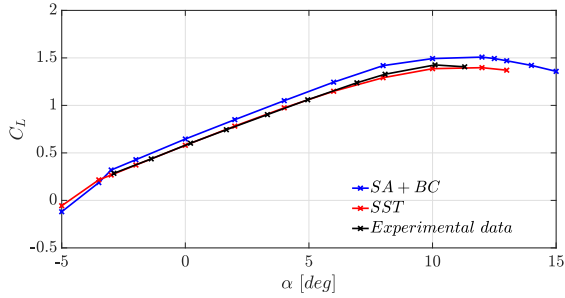


Figure 5.6: Polar at $Re = 61400$

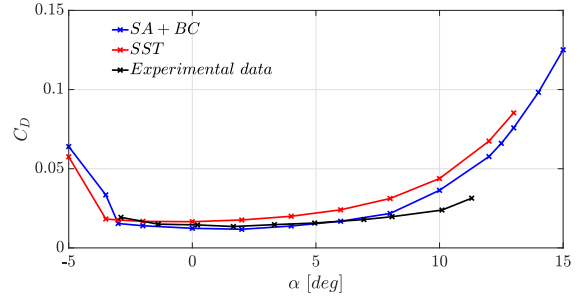
As it can be seen, there are significant differences in the prediction of the aerodynamic coefficients by the two turbulent models used. SA model with implemented transition shows better results than the SST model, with respect to the experimental data; the reasons for this discrepancy will be explained in Section 5.2.3.

5.2.2 $Re = 203100$

In Figure 5.7 the aerodynamic coefficients for the lower Reynolds number case are reported with respect to the angle of attack, while in Figure 5.8 the relative polar is shown.



(a) Lift coefficient



(b) Drag coefficient

Figure 5.7: Aerodynamic coefficients at $Re = 203100$

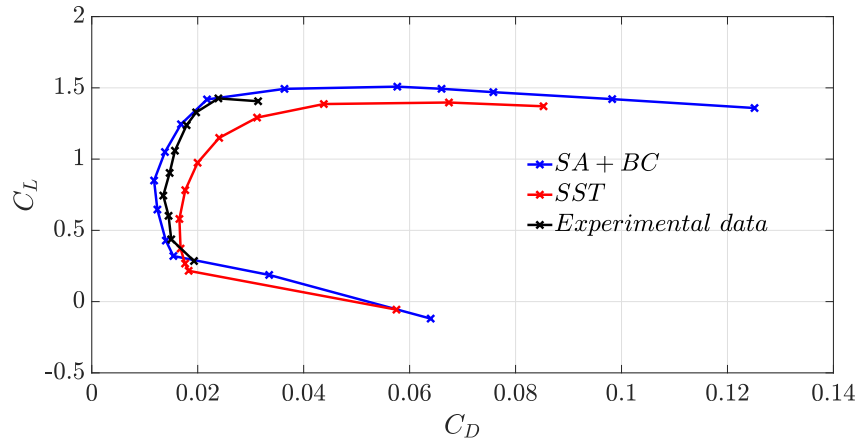
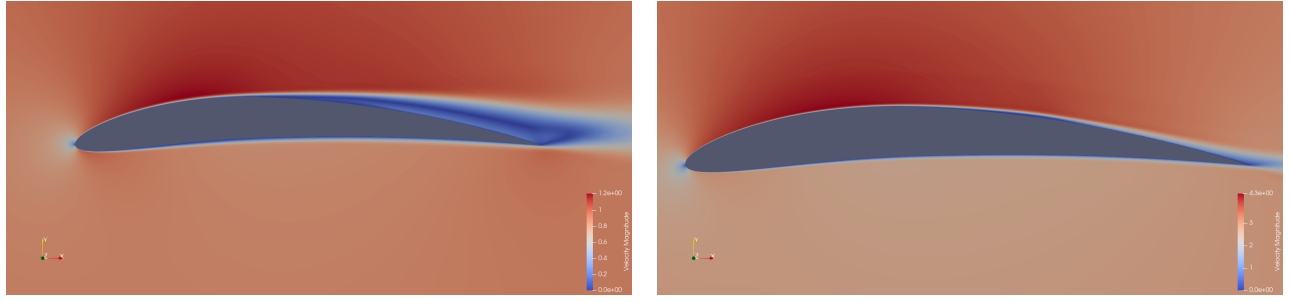


Figure 5.8: Polar at $Re = 203100$

As can be seen, with a higher Re , the two model curves get closer and fit better the experimental data; also this case will be examined in the following section.

5.2.3 Flow structure at $\alpha = 2^\circ$

In Figure 5.9, two visualizations at different Re are reported. As it can be seen, the flow at the lower Re , shown in Figure 5.9a, presents a separation on the upper surface of the airfoil, which can only be captured correctly by using a transition model. This separation can be related to the order of magnitude of the Re , which in this case is very low, leading to an open separation bubble. On the other hand, as can be seen in Figure 5.9b, the flow remains attached to the airfoil with an increased value of Re ; however, as shown in Figures 5.10 and 5.11b, a separation bubble is still present on the upper surface, but in this case the turbulent flow reattaches to the airfoil again as expected.



(a) $Re = 61400$

(b) $Re = 203100$

Figure 5.9: *Flow visualization at different Reynolds numbers. Velocity magnitude*

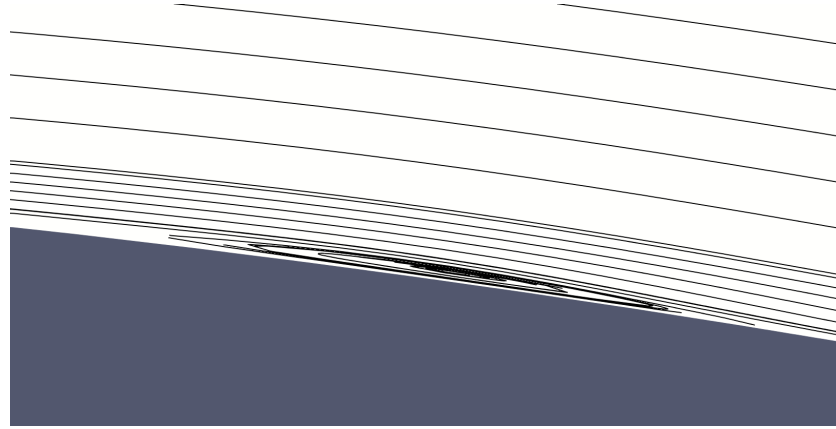


Figure 5.10: *Visualization detail of the laminar separation bubble at $Re = 203100$*

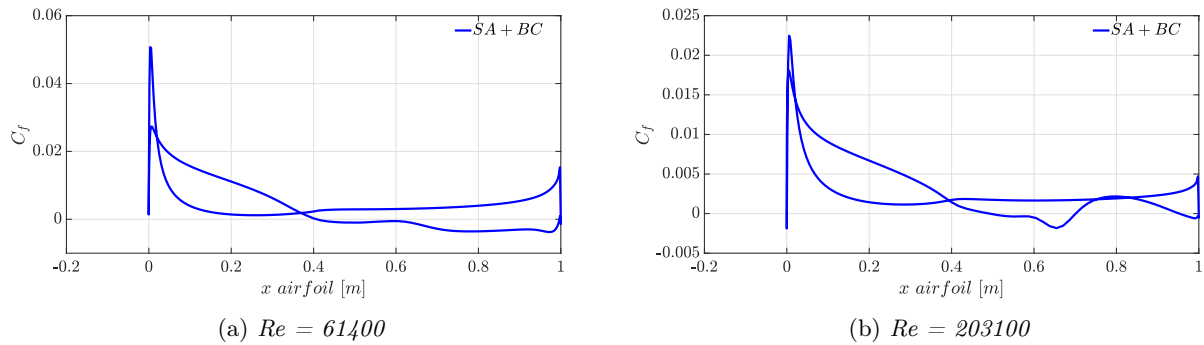


Figure 5.11: *Skin friction coefficients at different Re*

The generation of a separation bubble can only be predicted with a transition model. In fact with a fully turbulent model, such as SST, the flow remains attached for the entire length of the airfoil. This can be seen in the polar plots, reported in Section 5.2, especially in the lower Re case, where there is a discrepancy in the

aerodynamic coefficients between the SA model with transition and SST model: the latter predicts a higher value for the lift coefficient and a lower value for the drag coefficient.

5.3 Law of the wall

The theory behind the computation of the results for the Law of the Wall was discussed in Section 2.2.2. We only performed computations for a $Re = 203100$ with the grid and geometry depicted in Section 4.1, with further details on the domain discretization in Section 5.1. The numerical schemes used are exactly the same as the ones covered in Section 4.3, and the computations were carried out with both turbulence models: SA and SST, for the sake of comparison. All the data shown in Figures 5.12, 5.13 and 5.14 have been computed for an angle of attack of 2 degrees. The length of the normal line to the surface along which variables were calculated was 0.1, and 10.000 data points were generated along the lines.

5.3.1 SA model

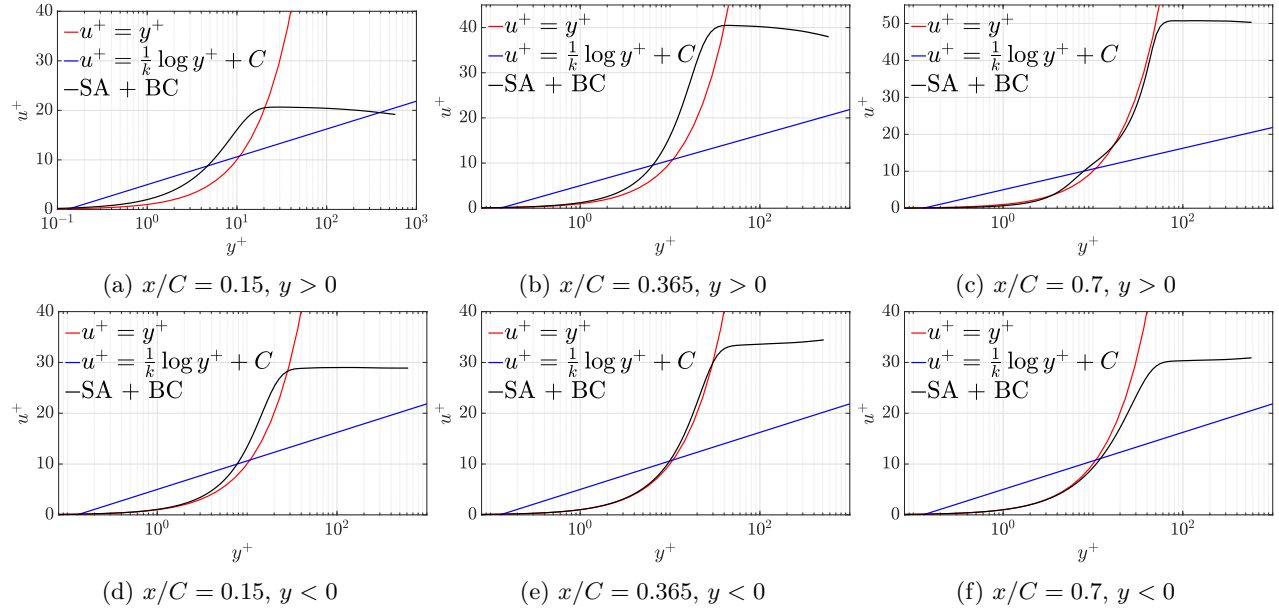


Figure 5.12: LOTW for $Re = 203100$ using SA

As may be seen in the figure above, our results approximate the theoretical predictions for the viscous sub-layer quite well, especially subplots (c), (e) and (f). This may owe to the fact that the boundary layer is sufficiently developed at that point. The discrepancies seen in subplots (a), (b) and (d) may be due to the fact that viscous stresses at the wall have not yet propagated fully throughout the boundary layer, and thus there is an increasingly higher overestimation of u^+ as y^+ increases. Moreover, in the case of subplots (a) and (b) another reason for the discrepancy might be the fact that the boundary layer is still laminar, given that transition is expected to happen when the flow reattaches after the laminar separation bubble (as corroborated by plotting eddy viscosity magnitudes in Paraview [13]).

However, it is worth noting that at no point does the trend in any of the conditions plotted shift to approximate the log-law. A thorough analysis into the potential sources of this pattern was undertaken. At first, it was

reasonable to hypothesize that the problem could be with the mesh, so we performed trials using finer and thicker boundary layer meshes with smaller first cell sizes and finer progressions. This resulted in negligible changes. After some trial and error, we decided not to pursue further this hypothesis, the main reason being that the original mesh could in fact solve u^+ correctly in the inner part of the boundary layer, as may be seen in the plots, so there was no reason to think that the intermediate and outer parts could be seriously miscalculated. The following step taken was to change the resolution of the plot over-line feature and the length of the normal lines. We then adopted a systematic approach to change parameters in the *.cfg* file and see their effect. The only significant change came from increasing the convergence criteria, but the trend remained similar. Finally, we resorted to the turbulent flat plate tutorial in SU2 ($Re = 5M$) and applied the setup of our configuration file to a flat plate (introducing some minor changes for compatibility with the mesh) to simulate the Law of the Wall and possibly rule out our *.cfg* setup as the cause of error. It came as a surprise when the results came out as they should. This left us with only one main cause of error: Reynolds number. After adjusting the first cell size to account for the changes in velocity and Re , we simulated again the NACA 6409 airfoil with a velocity of $80m/s$ and not changing the *.cfg* setup. The results are shown in Figure 5.13.

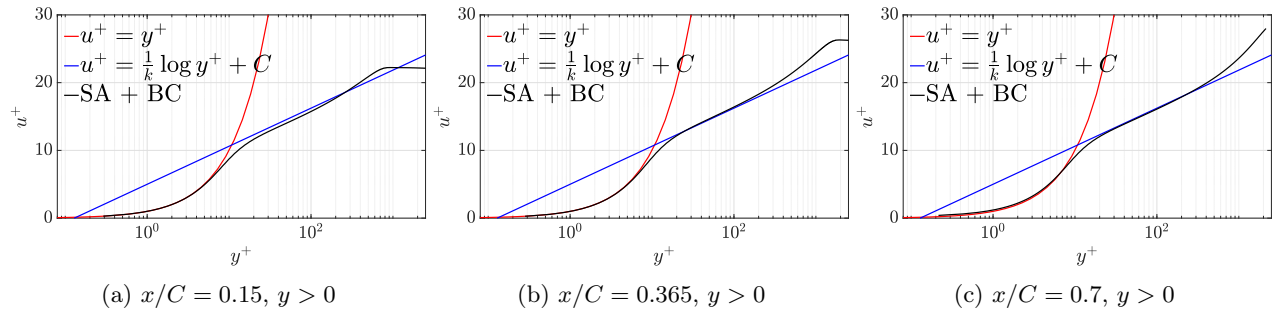


Figure 5.13: LOTW of the upper surface for $Re = 5288721$ using SA

The results from this trial were satisfactory for every chord-wise position tested. Recapping some turbulence theory, S.B. Pope states that if Re is large enough, an inner layer exists (the viscous-sublayer belongs to this layer) where the mean velocity profile is determined by viscous scales alone. In addition, even larger Re are required for the existence of an intermediate layer where the mean velocity profile depends on the viscous lengths alone. The log-law holds in this intermediate region, and therefore its existence will be bounded to the magnitude of Re [14]. This drove us to a clear conclusion: the reason why tend to capture correctly the viscous sub-layer while the log-law region shows an apparently anomalous trend owes to the low Re at which our tests are conducted. As such, the log-law is expected to form gradually as Re increases from a value of 203100.

5.3.2 SST model

The results for the Law of the Wall performed with the SST turbulence model without any transition model are quite satisfactory. A better approximation of the simulations with respect to the analytical expressions was expected, as the intrinsic usage of $k - \omega$ model in SST provides a better behaviour in near wall regions. On the other hand SA must rely on damping $\tilde{\nu}$ near the wall, which translates on a less accurate result. It would seem unintuitive to choose the SA model over the SST model judging by Figure 5.14 below. However, we have not chosen the SST model mainly because there is no compatible transition model available in SU2, which would preclude us from analysing reliably the effect of the turbulent trip on the transition from laminar to turbulent flow before the formation of a laminar bubble. Moreover, despite the Wilcox Roughness extension for $k - \omega$ is compatible with SST, as observed by Hellsten [15] and shown by Aupoix [16], when it is applied to SST, the velocity shift becomes underestimated for $k_s^+ > 30$.

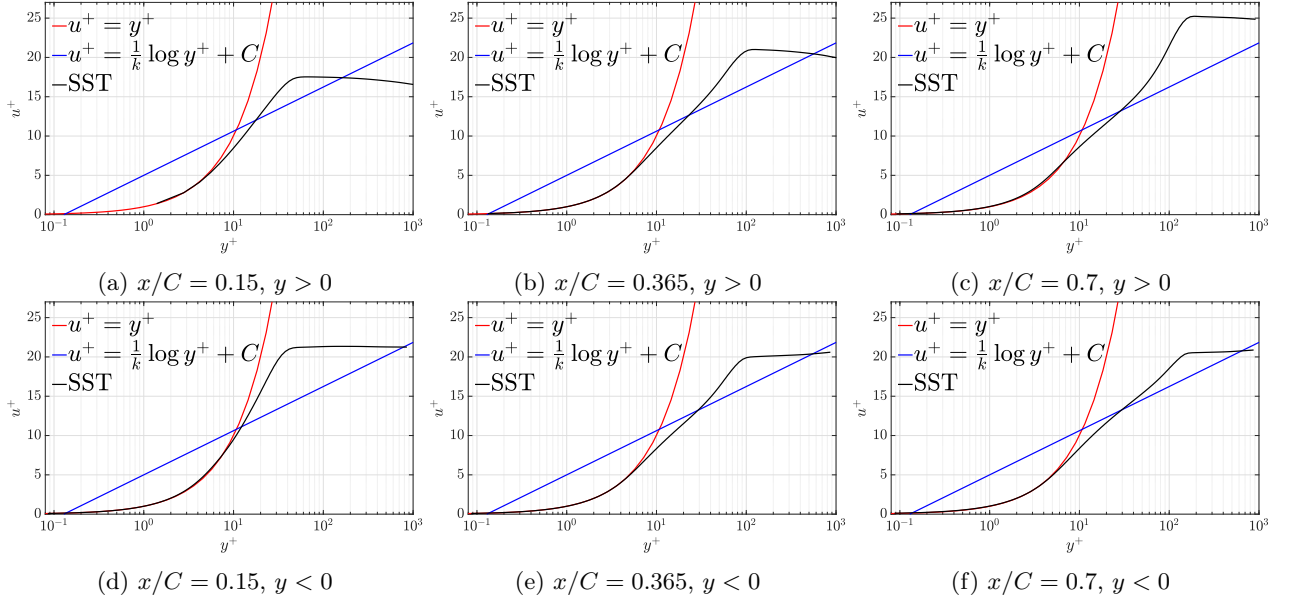


Figure 5.14: LOTW for $\text{Re} = 203100$ using SST

5.4 Optimization

In this section the results of the optimization are underlined. First of all the convergence of the optimization algorithm is reported for both configuration in Figure 5.15, as a function of the number of iteration.

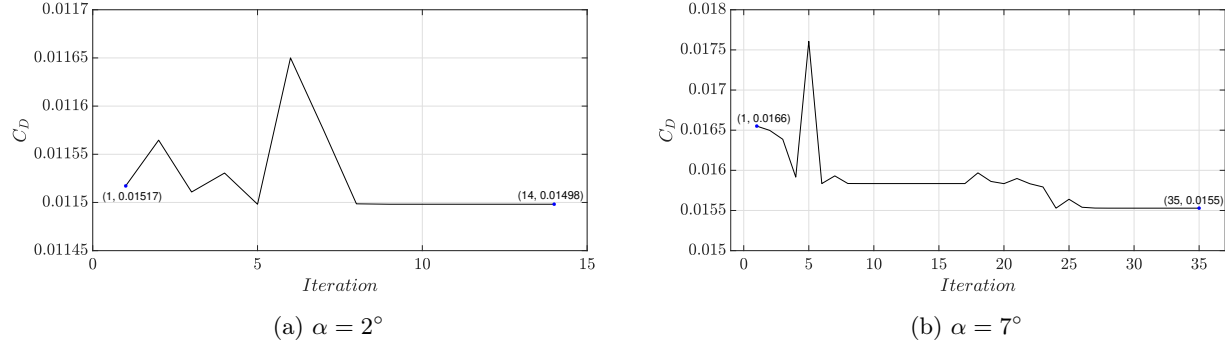


Figure 5.15: Optimization convergence

In Table 5.3 the results of the optimization are shown in terms of percentage of the reference value: Once the convergence is reached, the final mesh is tested with the free-stream properties described in Chapter 4. At this point a comparison between the base profile shapes and the optimized ones, shown in Figure 5.16; as can be seen, for the airfoil optimized at an angle of attack equal to 2° there are slight differences, while the airfoil optimized at higher angle of attack is changed in terms of chamber line and thickness; this new configuration leads to an higher positive angle of stall, as shown in Figure 5.17b, but at the same time, the negative stall occurs earlier, and a right shift of the drag curve, as shown in Figure 5.18b; the relative polars are reported in Figure 5.19.

| $\alpha[\text{°}]$ | $\Delta C_D[\%]$ | $\Delta E[\%]$ |
|--------------------|------------------|----------------|
| 2 | -0.17 | +0.0249 |
| 7 | -6.12 | +5.64 |

Table 5.3: *Optimization results*

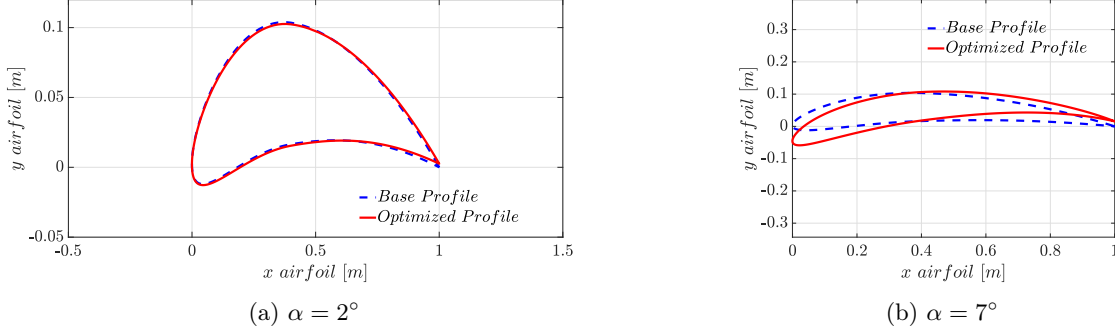


Figure 5.16: *Optimized airfoils*

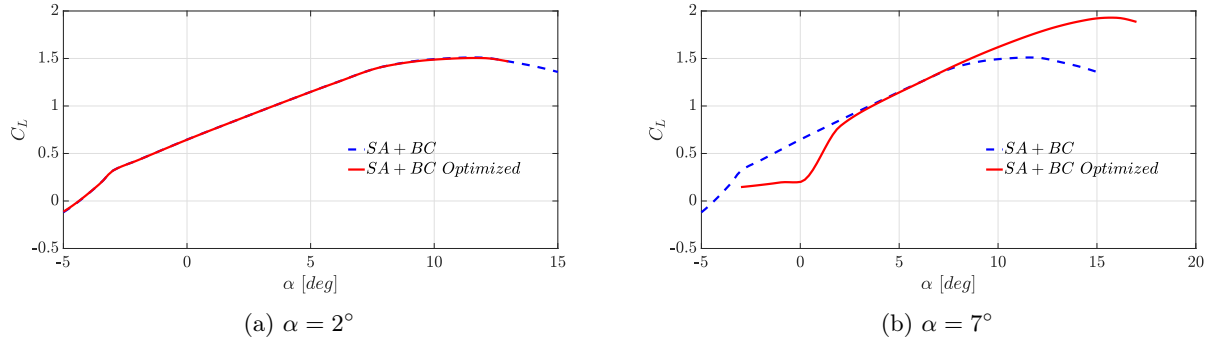


Figure 5.17: *Optimized lift coefficients*

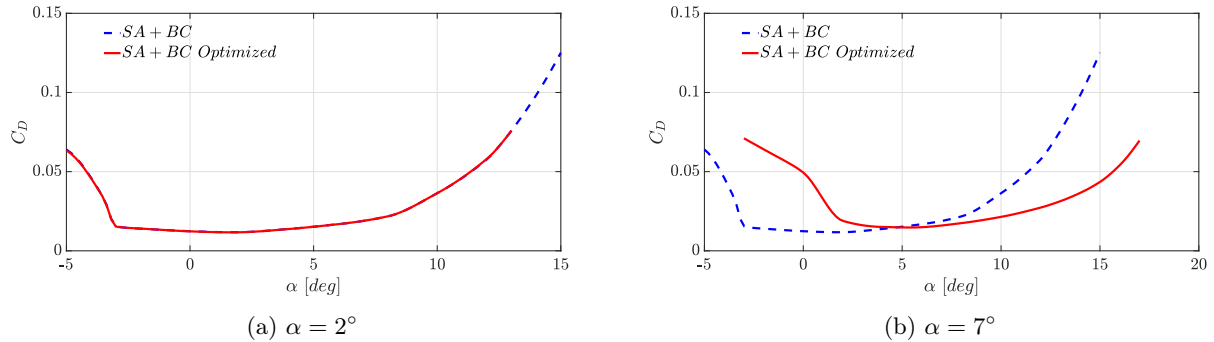
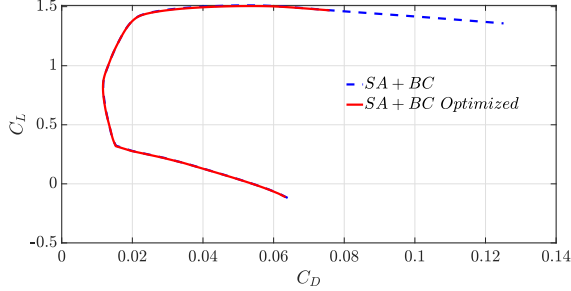
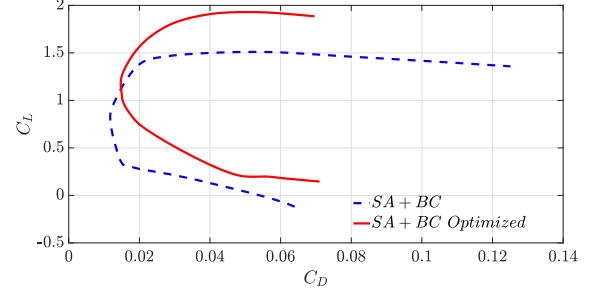


Figure 5.18: *Optimized drag coefficients*



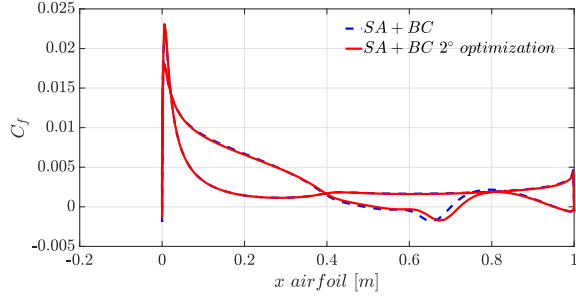
(a) $\alpha = 2^\circ$



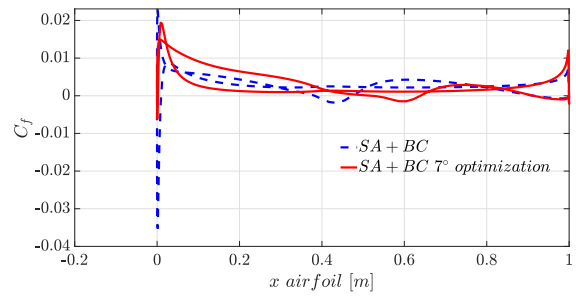
(b) $\alpha = 7^\circ$

Figure 5.19: *Optimized polars*

As can be seen in Figure 5.21 and Figure 5.20, the drag reduction is also caused by the translation of the laminar separation bubble towards the trailing edge; in the optimization at 2° , the transition happens slightly later than the baseline case ($\approx 1\%$ of the chord), while in the second case the transition occurs after $\approx 16\%$ of the chord with respect to the baseline case. This has a benefit effect on the lift performance of the airfoil, since at higher angle of attack the laminar separation bubble moves to the leading edge causing a separation in the main pressure recovery region and a consequent reduction of lift; if the bubble is sufficiently long, a possible stall can happen.



(a) $\alpha = 2^\circ$



(b) $\alpha = 7^\circ$

Figure 5.20: *Optimized skin friction coefficients*

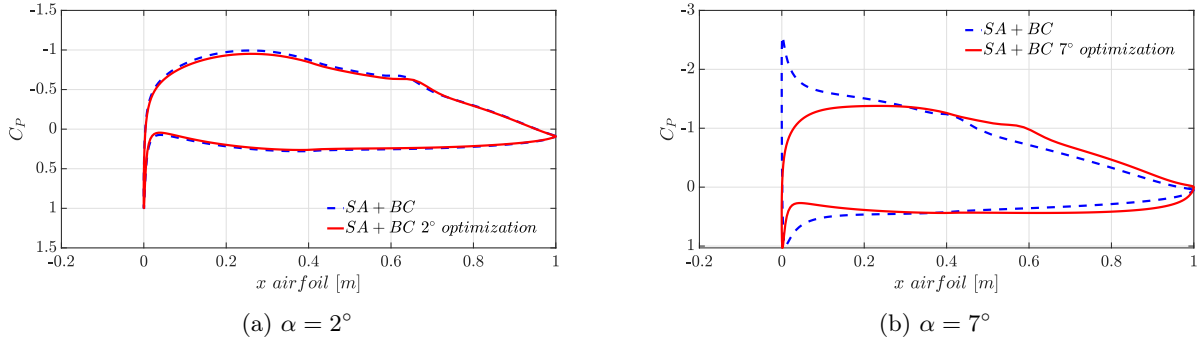


Figure 5.21: *Optimized pressure coefficients*

5.5 Roughness

In this section the results after the introduction of roughness are presented. The results for implementation of roughness on the complete airfoil are presented in Section 5.5.1, and the effects of localizing it on certain portions of the airfoil are presented in Section 5.5.2

5.5.1 Fully rough airfoil

As mentioned in Section 3.3, the aim of introducing roughness on the whole domain is to assess its numerical implementation and verify that we properly capture its effects. To do so, different k_s values have been studied at a fixed angle of attack of $\alpha = 2^\circ$. Note that the expression for the logarithmic region is no longer universal as for the clean case, but now depends on k_s^+ and therefore on the local C_f value (Equation 2.11). The Law Of The Wall at three different positions in the upper and lower surfaces ($x/c = 0.15, x/c = 0.365$ and $x/c = 0.7$ for k_s) and for values of 0.001, 0.006 and 0.012 are presented below:

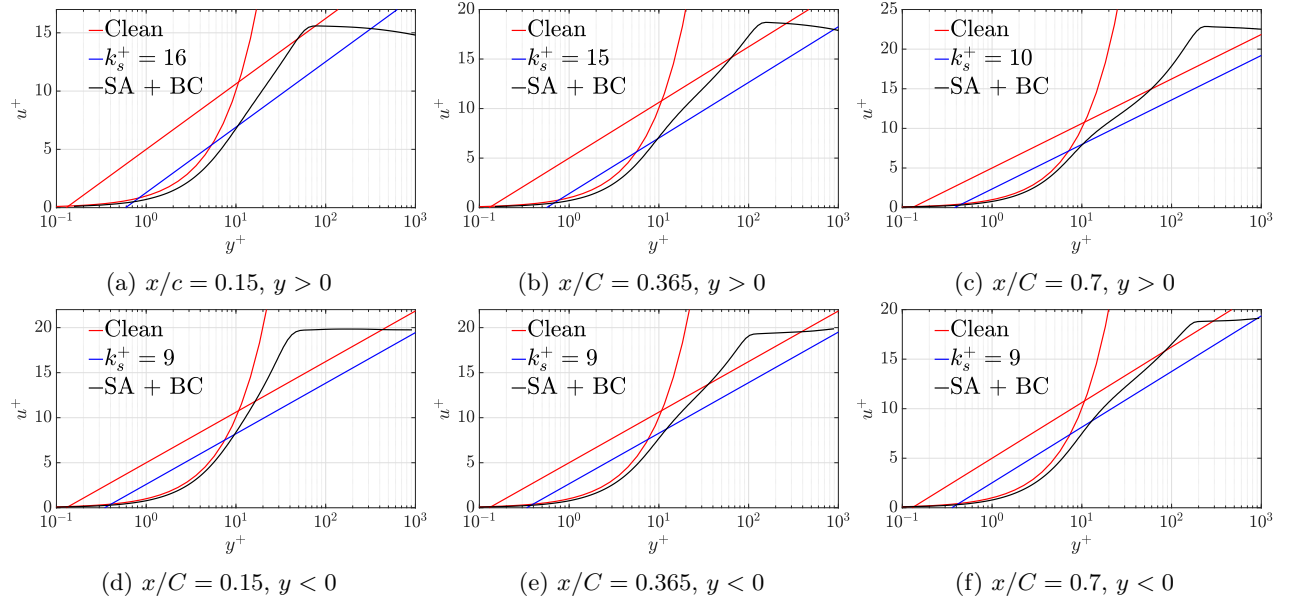


Figure 5.22: LOTW for $\text{Re} = 203100$ and $k_s = 0.001$

Regarding Figure 5.22 it can be seen how the k_s^+ values are far from the fully rough regime ($k_s^+ > 70$). Therefore the additive constant B in Equation 2.11 is no longer constant but dependent on k_s^+ , thus dependent on the local C_f value. As explained in Section 5.3, the Re used is not high enough for the logarithmic region to exist. Consequently, the results only approximate the analytical expression for the viscous sub-layer, departing from it progressively until reaching the freestream condition (flat behaviour for large y^+ values).

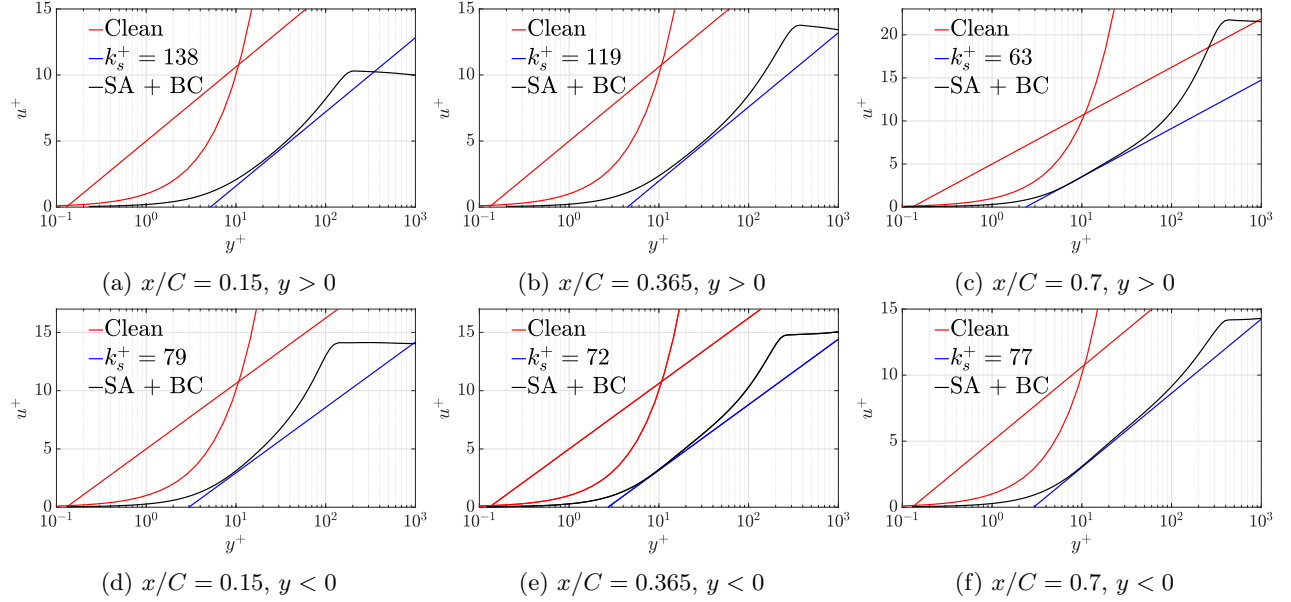


Figure 5.23: LOTW for $\text{Re} = 203100$ and $k_s = 0.000$

In Figure 5.23 it can be seen that after increasing k_s to 0.006, k_s^+ for all subplots except (c) belong to the fully-rough regime. Thus, the constant B in Equation 2.11 can be approximated to 8 as seen in Section 2.2.2. As expected, there is an appreciable trend as one moves towards the trailing edge in chord-wise position. Along the upper surface, the curve extends to higher values of u^+ and k_s^+ values decrease, both proportionally to the decrease in C_f . On the lower surface, the maximum values of u^+ and the values of k_s^+ do not vary as much because C_f shows a more uniform trend along chord-wise position.

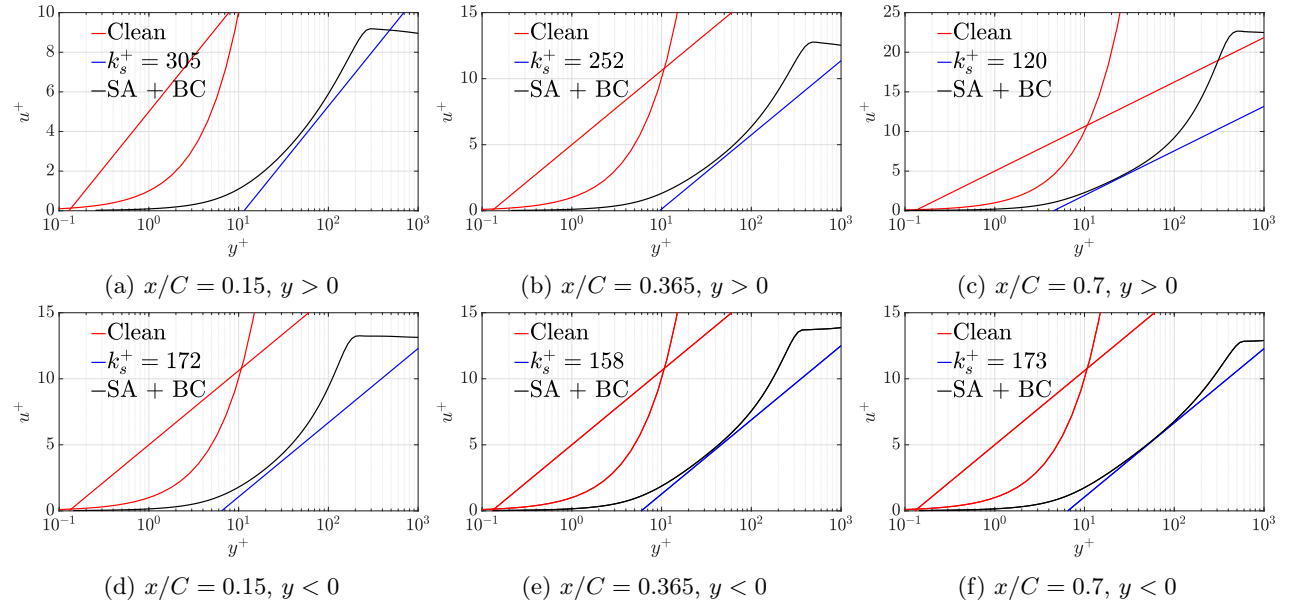


Figure 5.24: LOTW for $\text{Re} = 203100$ and $k_s = 0.012$

Figure 5.24 shows how all k_s^+ values now well exceed the threshold of $k_s^+ = 70$ for fully rough regime. The maximum value of u^+ and the values of k_s^+ follow the same trend as in Figure 5.23 due to their direct dependence on C_f , as may be observed in Figure 5.25. No further significant changes are observed with respect to Figure 5.23 because in both cases we are in the fully rough regime. Note that plots are done with respect to non-dimensional variables (u^+ , y^+ and k_s^+) which allows a direct comparison between these results.

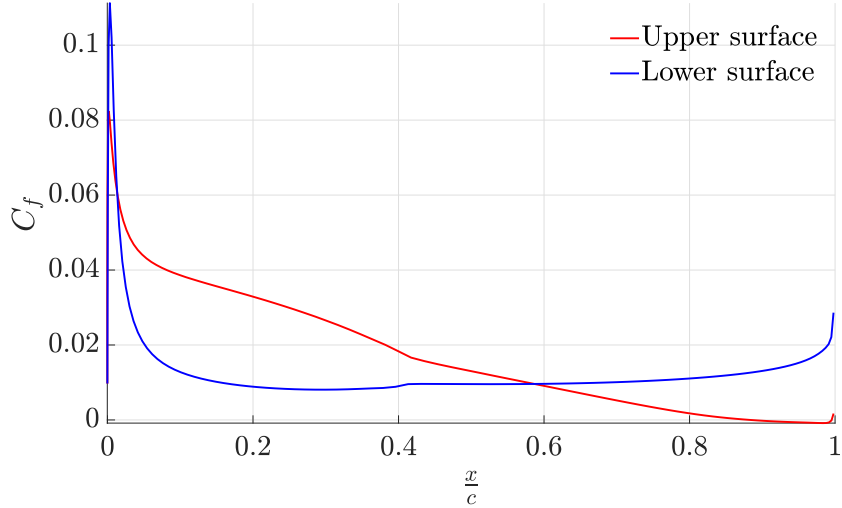


Figure 5.25: C_f distribution for $\alpha = 2$ and $k_s = 0.012$

5.5.2 Effects of localized roughness

This section presents a study of the effects on the overall lift-to-drag ratio of applying localised roughness along three different chord-wise positions on the upper and lower surfaces of the airfoil. The computational model for this part was described thoroughly in Section 4.1.2. The turbulent trip was positioned on both upper and lower surfaces at chord-wise positions ranging from $0.25 < x/c < 0.35$, $0.45 < x/c < 0.55$, and $0.70 < x/c < 0.80$. The values above were chosen to evaluate the effect of the turbulence trip on the flow pattern (and thus on the lift-to-drag ratio) at different positions. The width of 0.1 for the STRIP marker was chosen since we noticed that thinner trips would sometimes have a negligible effect in some combinations of chord-wise position and angle of attack.

For the upper surface, the value of $k_s = 0.001$ was not tested since in the fully rough airfoil, it yielded values below the fully rough regime threshold ($k_s^+ = 70$) for all chord-wise positions tested, both on upper and lower surfaces. In spite of this, we conducted some preliminary tests with $k_s = 0.001$ on the upper surface to realise that the efficiency always approximated the clean airfoil's but never surpassed it, which, together with the added time and computational cost entailed, led us to dismiss this roughness height. Nevertheless, performing the same preliminary tests on the lower surface, we noticed that the value of $k_s = 0.001$ would surprisingly give a higher value of efficiency for some angles of attack and for two different locations of the strip. Thus, this led us to consider such value of roughness height for the lower surface.

As may be seen in Figure 5.27 below, we have observed that for the turbulent trip positions on the upper surface, all the combinations of chord-wise trip position and angle of attack have detrimental effects on the efficiency, except for the position $0.70 < x/c < 0.80$, where the efficiency is increased by 9.18% for $\alpha = 10^\circ$, $k_s = 0.01$; and by 8.54% for $\alpha = 10^\circ$, $k_s = 0.005$.

For the turbulent trip positions on the lower surface, Figure 5.28 shows how all values of k_s tested give increments in efficiency for an angle of attack of 10° . The efficiency for $k_s = 0.001$ increases by 11.56%; for $k_s = 0.005$ increases by 9.57%; and for $k_s = 0.01$ increases by 9.25%. For the angles of attack ranging from 2° to 8° (both inclusive), the efficiency is only incremented for a roughness height of $k_s = 0.001$ and trip positions: $0.25 < x/c < 0.35$ and $0.70 < x/c < 0.80$. At 4° (the angle of attack for maximum lift-to-drag ratio), the efficiency

increases by 0.59%.

Figure 5.26a shows the C_f plot of one of these turbulators with $k_s = 0.01$ in the position $0.70 < x/c < 0.80$ on the upper surface. Despite the high value of roughness height ($k_s = 0.01$), the peak in C_f is not very pronounced. This owes to the fact that k_s^+ depends directly on C_f , which itself lowers as one moves towards the trailing edge. As such, a high equivalent roughness height causes a less significant increase in C_f as it would if it was located towards the leading edge. Figure 5.26b shows the C_f plot of another turbulator with $k_s = 0.001$ in the position $0.25 < x/c < 0.35$ on the lower surface, where a slight increase in C_f may be observed at that position. Since the value of equivalent roughness height is very low, the effect is barely noticeable.

A slight difference on the C_f coefficients with respect to the clean configuration at the separation bubble can be observed for both Figure 5.26a and 5.26b. We believe this difference is due to the modified number of iterations required when introducing the turbulence trip, which could also be noticed as the number of iterations grew with the value of k_s . By comparing subplots 5.26a and 5.26b, it can be observed how as k_s grows, a greater difference in the values of C_f is observed between the upper surface of the airfoil with the turbulator and the clean airfoil. Therefore, such increase in k_s causes the solution after a larger amount of iterations to change. This could be mitigated by increasing the threshold value for convergence or using another converge criteria such as an *RMS* value.

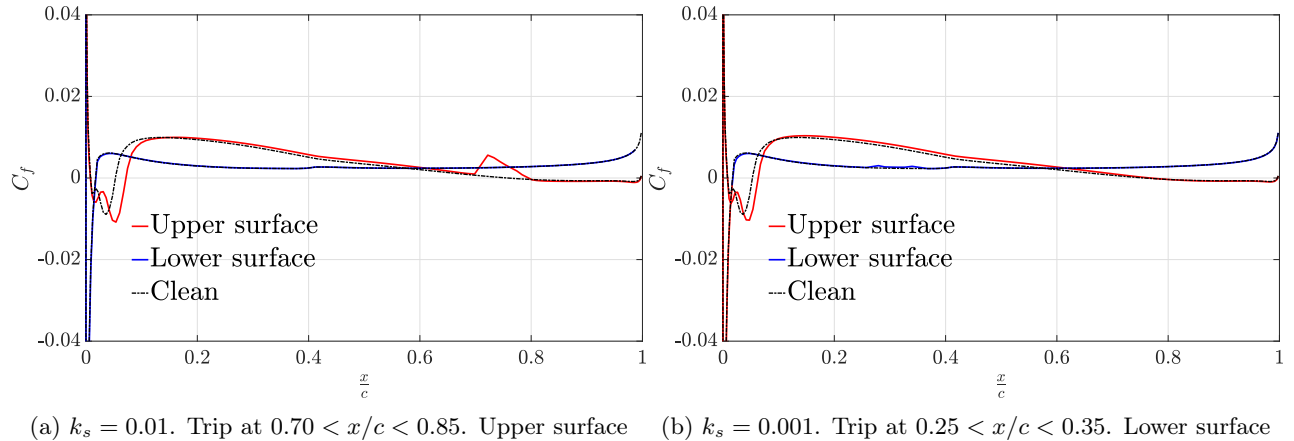


Figure 5.26: C_f plots at $\alpha = 10^\circ$

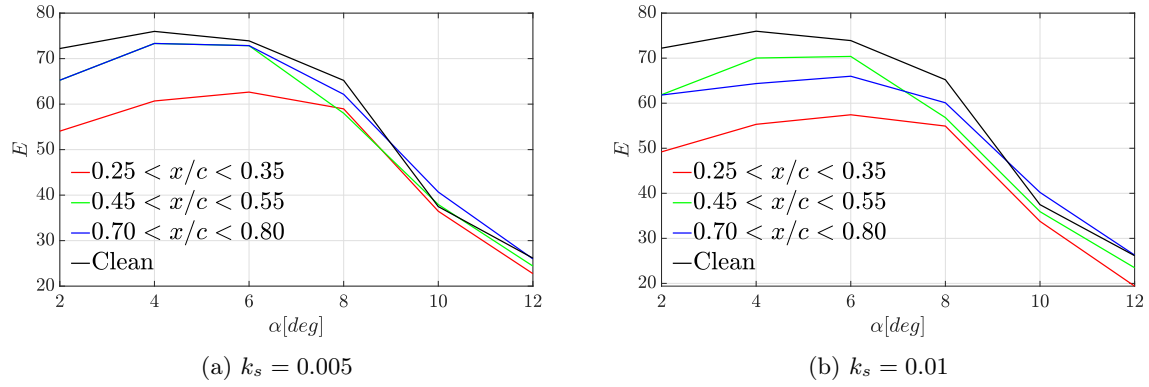


Figure 5.27: Efficiency comparison for strips at the upper surface

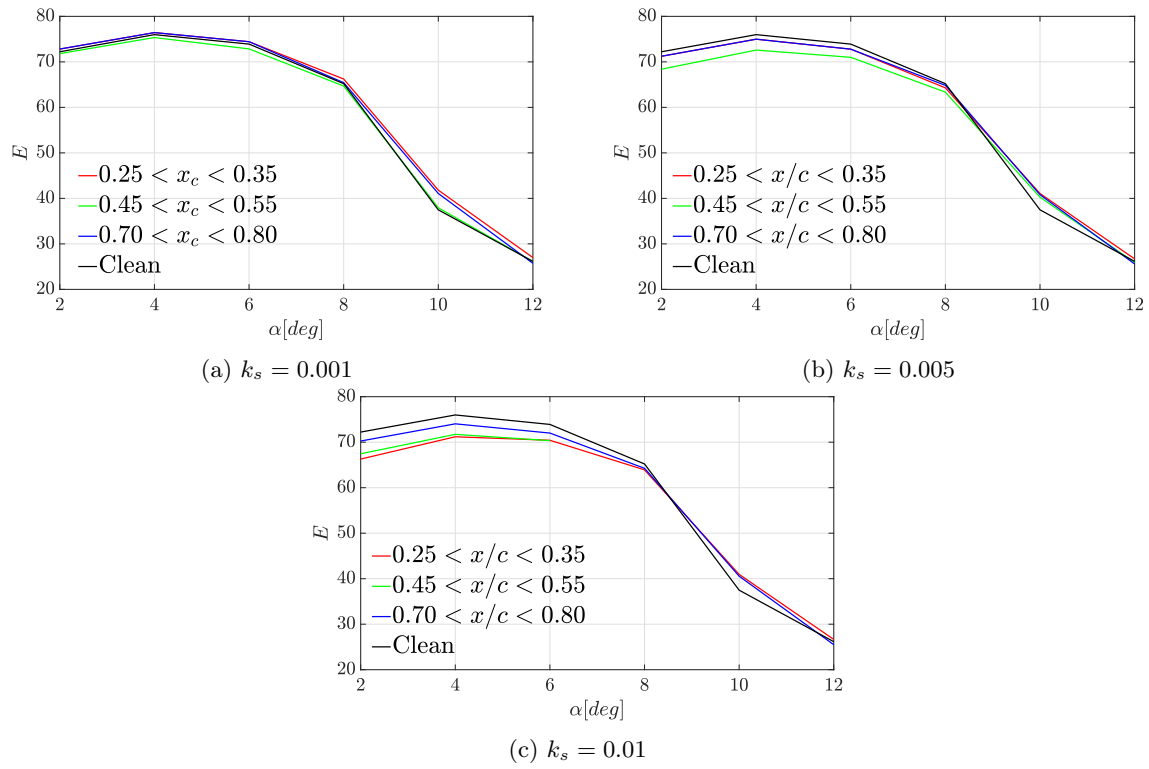


Figure 5.28: Efficiency comparison for strips at the lower surface

6. Conclusions

In the mesh convergence test, a study of the farfield discretization was conducted, fixing a farfield dimension of 120 m and a boundary element size equal to 4 m . In order to ensure enough accuracy in the simulations without compromising the computational cost of the simulations, the domain discretization analysis was performed. We concluded selecting the medium mesh with an expected $y^+ = 0.1$, which entails a first cell size of 0.00001 m and a growing rate of 1.1. Despite the relative error in drag coefficient was slightly high with the medium mesh, we deemed it appropriate since we could not establish a tight bound for the error, given that the separation region at that angle of attack was not negligible. Additionally, the computational cost that using a finer grid would entail drove us to this choice.

Regarding the plots of the Law of the Wall and the results of polars, SA+BC was chosen as the reference configuration for optimization and roughness analysis purposes given that SST underestimates drag at the lowest Reynolds number and overestimates it at the highest Reynolds number (as discussed in Section 5.2). In addition, there is no available transition model for SST, and the roughness extension for $k - \omega$ gives poor results when applied to SST.

6.1 Optimization

The results of the optimization in Section 5.4 feature the main property of a low Reynolds optimization carried out at low and high angle of attacks. In these conditions the flow structure, such as the position and length of the separation bubble, is very relevant in order to determine the final shape. While the optimization at low angle of attack (with respect to stall) shows light changes of the profile, as can be seen in Figure 5.16a, at 7°, shown in Figure 5.16b, these modifications are magnified. Globally it is possible to see a component of rigid rotation of the airfoil. Then, since the lower bound on the lift coefficient is fixed, a combination of camber-line and thickness at leading edge recovers part of the lift loss. In particular the shape of the leading edge is of a primary importance for the location of the separation bubble, which plays a fundamental role in drag reduction and lift recover, as explained in Section 5.4. In both cases it is possible to notice a drag reduction and an efficiency increment; the latter is a relevant parameter for a glider since the range, in gliding flight, is proportional to the efficiency. Even a slight increment of efficiency (as in the 2° optimization) means very higher range, if the initial altitude is consistent. In this regard, both optimized profiles shows a boost in the maximum efficiency (the related angle of attack is $\approx 2^\circ$). However it must be noticed that this analysis doesn't consider the drag inducted by the trailing vortices, which is a 3D effect. The effective efficiency can turn out to be different.

6.2 Roughness

Section 5.5.1 covered the implementation of roughness on the entire airfoil's surface for three different values of k_s . By plotting the Law of the Wall, we saw that for the lowest value of k_s , the k_s^+ values were far from the fully rough regime ($k_s^+ > 70$), which caused the constant B in Equation 2.11 to depend on k_s^+ , hence on the local C_f

value. Moreover, the results only approximated the analytical expression for the viscous sub-layer, departing from it progressively until reaching the freestream condition. For the higher values of k_s , we corroborated the strong dependency of k_s^+ and u^+ on C_f . Since plots were done with respect to non-dimensional variables (u^+ , y^+ and k_s^+) we could directly compare the results for the two highest k_s values to conclude that there were no remarkable differences in behaviour since the values of k_s^+ they both yield are decisively in the fully rough regime.

On the other hand, Section 5.5.2 examined the effects on the overall lift-to-drag ratio of applying localised roughness along three different chord-wise positions on the upper and lower surfaces of the airfoil. We may conclude that:

- For the turbulent trip positions on the upper surface, all the combinations of chord-wise trip position and angle of attack have detrimental effects on the efficiency, except for the position $0.70 < x/c < 0.80$, where the efficiency is increased by 9.18% for $\alpha = 10^\circ$, $k_s = 0.01$; and by 8.54% for $\alpha = 10^\circ$, $k_s = 0.005$.
- For the turbulent trip positions on the lower surface, all values of k_s tested give increments in efficiency for an angle of attack of 10° . The efficiency for $k_s = 0.001$ increases by 11.56%; for $k_s = 0.005$ increases by 9.57%; and for $k_s = 0.01$ increases by 9.25%. For the angles of attack ranging from 2° to 8° (both inclusive), the efficiency is only incremented for a roughness height of $k_s = 0.001$ and trip positions: $0.25 < x/c < 0.35$ and $0.70 < x/c < 0.80$. At 4° (the angle of attack for maximum lift-to-drag ratio), the efficiency increases by 0.59%.

Bibliography

- [1] Thomas D. Economou. *Constrained shape design of a transonic turbulent airfoil at a cte. C_L* . URL: https://su2code.github.io/tutorials/Turbulent_2D_Constrained_RAE2822/.
- [2] Michael S. Selig. *Low Reynolds Number Airfoil Design Lecture Notes*. 2003. URL: <https://m-selig.ae.illinois.edu/pubs/Selig-2003-VKI-LRN-Airfoil-Design-Lecture-Series.pdf>.
- [3] L. S. Roberts et al. “Forcing Boundary-Layer Transition on an Inverted Airfoil in Ground Effect”. In: *Journal of Aircraft* 54.6 (2017), pp. 2165–2172. DOI: 10.2514/1.C034304. URL: <https://doi.org/10.2514/1.C034304>.
- [4] Mark D. Maughmer, Timothy S. Swan, and Steven M. Willits. “Design and Testing of a Winglet Airfoil for Low-Speed Aircraft”. In: *Journal of Aircraft* 39.4 (2002), pp. 654–661. DOI: 10.2514/2.2978. eprint: <https://doi.org/10.2514/2.2978>. URL: <https://doi.org/10.2514/2.2978>.
- [5] Michael S. Lyon Christopher A. Selig et al. *Summary of Low-Speed Airfoil Data. Volume 3*. 1997. URL: https://m-selig.ae.illinois.edu/uiuc_lsat/Low-Speed-Airfoil-Data-V3.pdf.
- [6] Francesco Angelo Caccia. “Aerodynamic Performances of a Horizontal Axis Wind Turbine Blade in Icing Conditions”. PhD thesis. Politecnico di Milano, 2021.
- [7] A K Ravishankara, I Bakhmet, and H Özdemir. “Estimation of roughness effects on wind turbine blades with vortex generators”. In: *Journal of Physics: Conference Series* 1618.5 (Sept. 2020), p. 052031. DOI: 10.1088/1742-6596/1618/5/052031. URL: <https://doi.org/10.1088/1742-6596/1618/5/052031>.
- [8] B. Aupoix and Philippe Spalart. “Extensions of the Spalart–Allmaras turbulence model to account for wall roughness”. In: *International Journal of Heat and Fluid Flow - INT J HEAT FLUID FLOW* 24 (Aug. 2003), pp. 454–462. DOI: 10.1016/S0142-727X(03)00043-2.
- [9] Philippe Spalart. “Trends in turbulence treatments”. In: *Fluids 2000 Conference and Exhibit*. DOI: 10.2514/6.2000-2306. eprint: <https://arc.aiaa.org/doi/pdf/10.2514/6.2000-2306>. URL: <https://arc.aiaa.org/doi/abs/10.2514/6.2000-2306>.
- [10] Johann Nikuradse. *Laws of Flows in Rough Pipes*. Tech. rep. 1950. DOI: 10.1051/lhb/1951058. URL: <https://ntrs.nasa.gov/api/citations/19930093938/downloads/19930093938.pdf>.
- [11] Hermann Schlichting and Klaus Gersten. *Boundary-Layer Theory*. 9th ed. Springer-Verlag Berlin Heidelberg, 2017, pp. XXVIII, 805. DOI: <https://doi.org/10.1007/978-3-662-52919-5>. URL: [http://ae.sharif.edu/\\$%Csim\\$viscousflow/Schlichting%20-%20Boundary%20Layer%20Theory.pdf](http://ae.sharif.edu/$%Csim$viscousflow/Schlichting%20-%20Boundary%20Layer%20Theory.pdf).
- [12] Andy P. Broeren Michael S. Selig James J. Guglielmo and Philippe Giguere. *Summary of Low-Speed Airfoil Data. Volume 1*. 1995. URL: https://m-selig.ae.illinois.edu/uiuc_lsat/Low-Speed-Airfoil-Data-V1.pdf.
- [13] Sandia National Laboratories. *SU2*. Version 5.10.0. URL: <https://www.paraview.org/>.
- [14] Stephen B. Pope. *Turbulent Flows*. Cambridge University Press, 2000. DOI: 10.1017/CBO9780511840531.
- [15] A. Hellsten and S. Laine. “Extension of the k-omega - SST Turbulence Model for Flows over Rough Surfaces”. English. In: *AIAA Atmospheric Flight Mechanics Conference, New Orleans, Louisiana, August 11-13, 1997*. 1997, pp. 252–260.

- [16] B. Aupoix. “Wall Roughness Modelling with k-w STT Model”. In: *10th International ERCOFTAC Symposium on Engineering Turbulence Modelling and Measurements*. MARBELLA, Spain, Sept. 2014. URL: <https://hal-onera.archives-ouvertes.fr/hal-01071701>.

7. Appendix A: Resources

In order to simplify the organization of the different files used during the project a GitHub repository has been created. The link to the repository is : <https://github.com/nilcpolimi/CFD-Project-Team-18>.

The organization of the repository is the following:

- **Common part:** This folder contains the information of the common part of the project, thus up to the computation of the LOTW for the clean case (inclusive). In first place, the script used to discretize the airfoil (*Airfoil_points.m*), the set of three meshes used for grid convergence (*mesh_coarse.geo*, *mesh_media.geo*, and *mesh_fine.geo*), the final configuration chosen (*Mesh_baseline.geo*) and the final *SU2 config* file (*Config_Baseline.cfg*) are presented. In addition, the scripts to plot the polars for both *Re* studied are also included (*Polar_203100.m* and *Polar_61400.m*). Finally, the script used to compute and plot the LOTW is also included (*LOTW.m*).
- **Optimization:** This folder contains two different configuration files that are required to run the optimization: the former (*config_box(part1).cfg*) is used to write the FFD box around the airfoil presents in the mesh input file, while the latter (*config_optimization(part2).cfg*) is used by *shape_optimization.py* in the optimization loop; different angles of attack are expressed in terms of velocity components in the same configuration files. In this folder there is also a mesh file (*mesh_media.geo*), set as the input of the optimization algorithm.
- **Roughness:** This folder contains information related to introduction of roughness. For this reason, it has been divided in two folders: Full rough and Strip. In the Full Rough folder it can be found the *config* file with roughness applied on the whole airfoil, as well as the mesh used for the baseline *Re* and the one used for *Re*=5M (*Mesh_baseline.geo* and *mesh_highRe.geo* respectively). In addition a modified version of the LOTW script in order to account for the modification of the analytical expressions is included (*LOTW.m*). Regarding the folder Strip, an example of how the strip was defined in the mesh is presented (*mesh_strip_0.7-0.8.geo*). As it will be commented later, different meshes were generated to account for every position in the upper or lower surface, but as the general structure is the same they've not been uploaded. The *config* file to run these meshes is also presented (*config_media_transition_strip.cfg*). Finally the script used to assemble the aerodynamic coefficients for every strip configuration (*assemble_efficiency.m*) and the script used to plot the efficiency comparison (*Plot_efficiency.m*) have been included.

Additional files were used; for example to simulate each angle of attack of the polar the *config* file required a modification of the components of freestream velocity. However, as these involve minor modifications and the general structure is always the same, they have not been included in the repository.